Shore-parallel Sediment Transport by Waves and Tides in Inner Shelf Waters

by

Alice Pistolesi

Submitted to the Department of Civil and Environmental Engineering
in partial fulfillment of the requirements for the degree of

Master of Engineering in Civil and Environmental Engineering

at the

MASSACHUSETTS INSTITUTE OF TECHNOLOGY

June 2016

Signature of Author: Signature redacted

Alice Pistolesi
Department of Civil and Environmental Engineering
May 12, 2016

Certified by: Signature redacted

Ole S. Madsen
Donald and Martha Harleman Professor Emeritus
Thesis Supervisor

Accepted by: Signature redacted

Heidi Nepf
Donald and Martha Harleman Professor of Civil and Environmental Engineering
Chair, Graduate Program Committee

Shore-parallel Sediment Transport by Waves and Tides in Inner Shelf Waters

by

Alice Pistolesi

Submitted to the Department of Civil and Environmental Engineering On May 12, 2016, in Partial Fulfillment of the Requirements for the Degree of Master of Engineering in Civil and Environmental Engineering

Abstract

In shallow waters the combined action of waves and currents significantly affects the motion of sediment on the bottom, and hence the nature and phase of their interactions with each other contribute to the shaping of the beach. Using pressure and velocity data collected just outside the surfzone (in two meters depth) on the south shore of Martha's Vineyard, MA, we compared the variations in net alongshore transport during different wave-current conditions, studying the effect of the wave-current phase to show that it can have a significant impact on transport rates in shallow water conditions. Three distinct intervals were looked at in particular, representing respectively neap tide, calm conditions, spring tide, calm conditions, and spring tide, storm conditions. For each of these time intervals wave and current characteristics were computed and presented.
Water depth, wave height and period and were obtained from the pressure data using linear wave theory and wave orbital velocity was computed using two different approaches: one based on gross characterisation of the wave conditions and treating them as a bulk, the other from spectral analysis of the surface spectra. These results were shown to have very good agreement with the same wave characteristics obtained from the velocity data. Current characterization was also computed from the velocity data. These were shown to be dominantly tidal and hence we focused our interest on identifying a similar signature in the slow-variation of the waves to correlate the two.

Based on the results from the hydrodynamic analysis, an estimate of the net transport rate was made, assuming a 90° angle between the waves and the currents, for each of the three scenarios, highlighting the effect of varying wave shear velocity and net sediment transport rates. To further understand the impact of the wave-current phase, a fourth analysis was performed on synthesized data (based on real data) in which the phase could easily be altered. These calculations showed how accounting for this phase-shift greatly altered the sediment transport, and how it is affected by increased wave velocity due to meteorological conditions.

Thesis supervisor: Ole S. Madsen
Title: Donald and Martha Harleman Professor Emeritus

Contents

List of Figures

List of Tables

1 Introduction

1.1 Background

The importance of sediment transport in shaping our coastlines has become widely accepted in the last fifty years (*Lou and Ridd*, 1997), and thus has led to increasing research in the coastal engineering field. With growing populations and expansion of human activities closer to the shoreline as well as a decreased return period of large storms due to climate change (*IPCC*, 2014), understanding beach erosion has become a pressing issue which can ultimately lead us to improved engineering solutions and a more sustainable settling of human population in these environments. Indeed, the economic attractiveness of coastal areas, which bring in trade through the ports, tourism through recreational resorts and infrastructures, food through fisheries or even security as bases for naval forces and natural borders (*Dean and Dalrymple*, 2004), means that their development is likely to continue expanding, regardless of the environmental risks associated with them. The costs associated with previous losses, both of infrastructure and livelihood, from meteorological events such as Hurricane Katrina in 2005 to the floods in the Bay of Bengal following monsoons, have however put pressure on governments to increase spending on coastal protection structures and to implement new policies regarding the location of infrastructures relative to the shore.

Despite the large geographical variability in coastlines, and the different wind, wave and current conditions, the beach-shaping physical processes are very similar worldwide. Sediment transport of importance and consequence to the coastal engineer occurs in the surfzone (*Tajima and Madsen*, 2005), in which the waves reach shallower depths and start breaking thereby mobilizing the bottom sediments. These destabillized sediments are then picked up and displaced by longshore currents (both those generated by the transfer of momentum from the incoming oblique waves (*Longuet-Higgins*, 1970) and the tidal currents which are part of the ambient conditions, as shown by *Inman et al.* (1968)). This transport requires action from both the waves and the currents together as the former, "feeling" the bottom more strongly than the latter and thus associated with a greater bottom shear stress, cannot transport the sediment effectively (especially before breaking, when the waves still behave in a linear fashion and orbital velocity is symmetric between the troughs and the crests). Currents on the other

hand, cannot instigate sediment motion but, being unidirectional over a wave period, cause net transport in the longshore direction (*Grant and Madsen*, 1979). This combined action is further enhanced in the bottom layer of the water column, where both currents and waves influence each other leading to modified shear stresses and velocities. This affects the bathymetry of the seafloor, which feeds back into the original physical properties of the waves and currents (*Grant and Madsen*, 1979). From these observations it becomes obvious that understanding how the relationship between waves and currents affects sediment transport is incredibly important. These interactions are amplified during storms, which is when the bulk of transport and hence of beach erosion occurs. This is due to the generation of an offshore undertow current by the increased volume of water heading shoreward (*Svendsen*, 1984), coming from the larger wind induced waves, leading to offshore sediment transport (*Hoefel and Elgar*, 2003). In these instances the effect of waves on longshore currents is expected to be even stronger, and hence affects both longshore and cross-shore sediment transport.

Once sediment motion is instigated, two types of transport can be distinguished: bedload and suspended load. There is no direct transition between the two modes, but it is generally considered (*Bagnold* , 1966; *van Rijn*, 1984) that bed-load is controlled essentially by gravity forces, preventing particles from rising further up in the water column and consisting of a combination of rolling, sliding and saltation of sediment grains along the bottom. Suspended load on the other hand, is dependent mostly on turbulent eddies (*van Rijn*, 1984) and lift forces (*Amoudry and Souza*, 2011). It is initiated when the combination of these two agitations is greater than the weight of the particles (*Amoudry and Souza*, 2011), entraining them above the bed into suspension for as long as the vertical eddy velocity is greater than the particles' fall velocity (*Bagnold* , 1966). Direction is another characteristic of sediment transport and can occur crosshore or alongshore with longshore transport driven by currents being considered to be the main contributor to long-term topographical changes. Cross-shore transport is associated with much larger and more sporadic displacements of sediment as it is mostly induced by the undertow from storm waves. This seaward current removes the sediment from the surfzone into deeper water causing erosion of the system. Whilst the long-term effect of this removal has been argued to balance out over time (*Zhang et al.*, 2002), the beach recovery process can take up to decades and the moving mechanism of sediment towards the shore is still uncertain (*Zhang et*

al., 2002; *Komar*, 1998). Hence on these timescales (5-10 years) it is considered that the storms cause permanent removal of sediment from the shore and hence cannot be neglected, especially in uniform wave conditions which cannot contribute to shoreward movement (*Tajima and Madsen*, 2005). Predicting and modelling sediment transport has proved to be very challenging due to the difficulty in obtaining reproducible field data (*Dean and Dalrymple*, 2004): beach profiles can be determined from which sediment accumulation or decline is extrapolated, however factors such as tidal variation within the survey duration or wave motion can affect the results, and usually lead to depth errors of up to 20 centimeters. More modern technologies including use of GPS or Lidar (LIght Detection And Ranging) have enabled more precise measurements over wider areas, decreasing the depth error down to three centimeters in some instances (*Dean and Dalrymple*, 2004; *Irish and Lillycrop*, 1997). Another approach has involved surveying the evolution of tracers injected in sand grains (*Wang et al.*, 1998; *Duane*, 1970) and assessing their overall transport. In more recent years an emphasis has been put on 2D and 3D numerical modelling of time-varying sediment transport, highlighting the vast amount of approaches used. *Amoudry and Souza* (2011) have reviewed a few of the models available, as well as the differences in mathematical formulations these have been using. As well as varying spatial resolutions (from "local" scale, to long-shore behaviour along large stretches of coastlines), models simulate sediment transport over different vertical resolutions, including depth-averaged. However all of these methods are subject to variations in the ambient conditions such as mean sea level (due to tides), meteorological conditions and resulting non linear interactions between waves and currents or bottom topography (such as the presence and shape of ripples) (*Camenen and Larroudé*, 2003). The difference in timescale between wave-current interactions in the bottom boundary layer (seconds to hours) and those over which bed morphological changes can be observed (weeks to years) is one of the constraints coming from the environmental influence and the time variation of the model. To account for this difference many coastal models make use of a morphological acceleration factor, which is used to scale the bed level changes at each computational time step, allowing them to change simultaneously with the hydrodynamics (*Delft Hydraulics*, 2007; *Li*, 2010). This may lead however to over approximating conditions within the time frames studied and hence missing out on wave condition changes within a tidal cycle when modelling on the scale of a few hours, or on tidal variations when

studying the bed evolution over several months (*Amoudry and Souza*, 2011; *Delft Hydraulics*, 2007). It has been equally complicated to obtain near bottom flow velocity measurements, as well as accurate bed roughness (*Grant and Madsen*, 1979), both of which are required when computing sediment transport. Following these uncertainties in data acquisition, a wide variety of formulae have been established to compute sediment transport in shallow waters: some fit to individual datasets, others purely theoretical.

1.2 Objectives

The objective of this project is to study longshore sediment transport owing to dominantly cross-shore waves and longshore tidal currents conditions before the former have a chance to break, in order to gain a better appreciation of their relative importance and interactions. By comparing hydrodynamic conditions between neap and spring tides, as well as between average and storm conditions, we hope to observe changes in the wave behaviour which we can then correlate to changes, if any, in the sediment transport. Indeed, between the neap and spring tides we want to show that the net transport would be different as the greater tidal amplitudes would have an impact on current velocity and hence on current shear velocity (one of the controls of bedload transport) and thus make them vary within the tidal cycle. Equally, during a storm the wave velocities would be expected to increase, translating to higher wave bottom orbital velocities and thus affecting the wave-current interaction in the bottom boundary layer.

1.3 Outline

In order to compute the sediment transport we used field data to obtain the wave and current specifications needed. Section 2 discusses the environment in which this data was collected and describes its analysis. The hydrodynamic characteristics obtained were input into a physics based theoretical sediment transport model based on wave-current interactions. This model, detailed in Section 3, was applied to various scenarios in which these interactions were differently correlated according to the conditions observed from the field data. Their effect on net sediment transport is summarised in Section 4.

2 Field Data Analysis

2.1 Field Data Collection Site

2.1.1 Hydrodynamic characteristics of the location

The field data was collected in July and August 2014, from sensors placed in about two meter water depth along the south coast of Martha's Vineyard, MA. The sensors were deployed on either side of Katama Inlet, with two on Wasque Point and three on Norton Point (see Figure 2.1.1). Tides are taken throughout this project to be incoming (or flooding) when going into Katama Inlet and the Vineyard Sound through Muskeget Channel, and outgoing (or ebbing) when coming out of these two areas. The

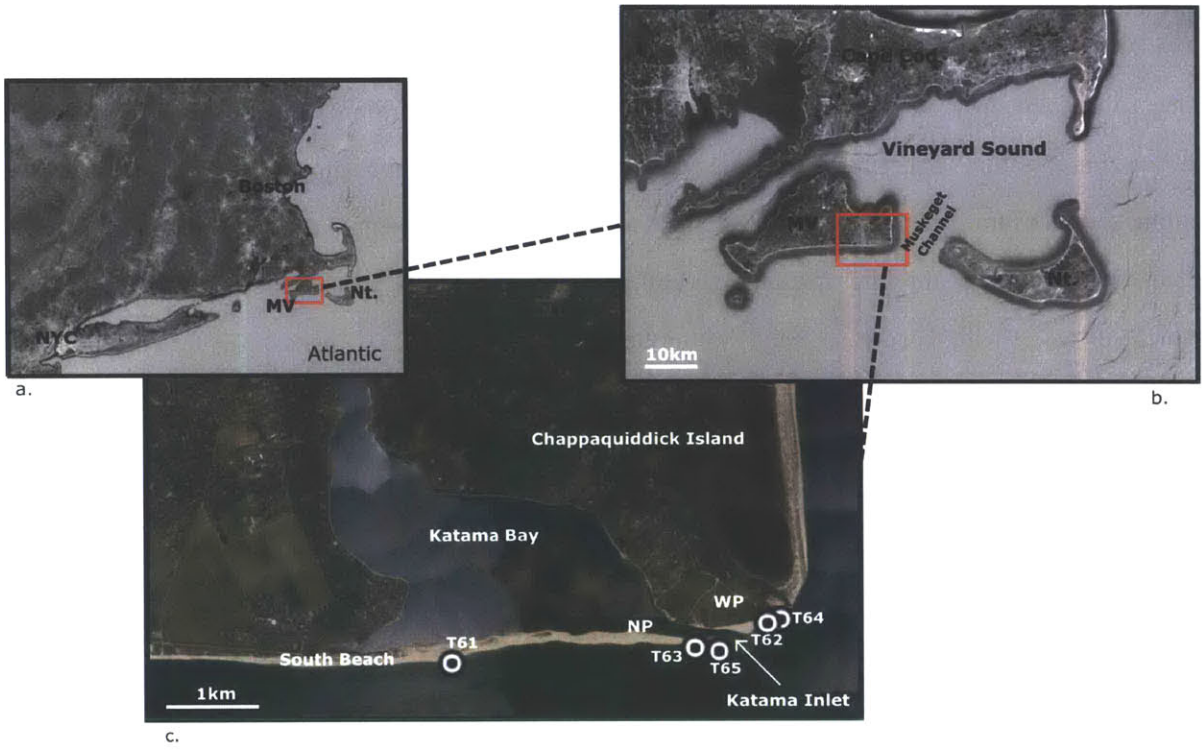

Figure 2.1.1: Geographical location of the study site and of the ADV and pressure sensors deployed in the summer 2014. Maps **a** and **b** give an overview of the general area, and identify the bodies of water which have a key role in the hydrodynamics around Katama Bay. Map **c** locates the sensors relative to each other and to the inlet. From this positioning, T61 was expected to be the least affected by the inlet and hence used as a reference. NYC-New York City, MV-Martha's Vineyard, Nt.-Nantucket, WP-Wasque Point, NP-Norton Point. *From GoogleEarth.*

area is characterized by strong bathymetric variations, especially around Wasque Point, as well as by the migrating Katama Inlet, which has been moving eastward since 2007 to its current position on the Chappaquiddick Island side of the Edgartown Channel. The inlet follows a ten-year cycle over the course of which it breaches, migrates and closes before starting again. The mechanics behind this periodic behaviour are not yet fully understood, nor is the correlation with the coastal erosion on Wasque Point. However, the presence of the Muskeget Channel between Martha's Vineyard and Nantucket has been shown to generate highly asymmetric currents. Ebb tides behave like jets coming out of the Vineyard Sound, past Chappaquiddick Island and therefore generate a steep velocity gradient with magnitudes decreasing rapidly westward, away from the main jet's southward direction. When these tidal currents flip, they flow along the south shore of Martha's Vineyard in the easterly direction into the channel and the Sound (J. Hopkins, personal communication, April 2016). This asymmetry means that there are virtually no currents flowing past South Beach (where the sensors are positioned) during the ebb tide. The periodic progression of the inlet shown in Figure 2.1.2 however suggests strong sediment transport along the shoreline, and predominantly oriented towards the east. There is a yearly migration of the inlet towards the east and Chappaquiddick Island (Figure 2.1.2 **a** until **d**), which correlates with a decrease in the size of the opening between 2007 (its last closure episode) and today. This is a natural consequence of the easterly-dominated tides described above: as the sediments are displaced by asymmetric currents, more sediment will be transported in the stronger, i.e. easterly current direction. The combination of the flows coming out of Katama Inlet disturbing the sediment transport just offshore of it, with the rapid erosion of Wasque Point (becoming more angular with the years, reaching a near 90°in 2012 (Figure 2.1.2 **e**), up until **f** when the inlet closes and the Point starts smoothing out again) lead us to expect complex sediment fluxes in the area, acting in both cross-shore and longshore directions.

2.1.2 Data collection

At each of the five studied locations a pressure sensor and a 10MHz Sontek Triton ADV (Accoustic Doppler Velocimeter) were deployed and recorded, over the course of the survey, pressure and velocities in the north-south and east-west directions. The two sensors, located at 48 cm and 79 cm above

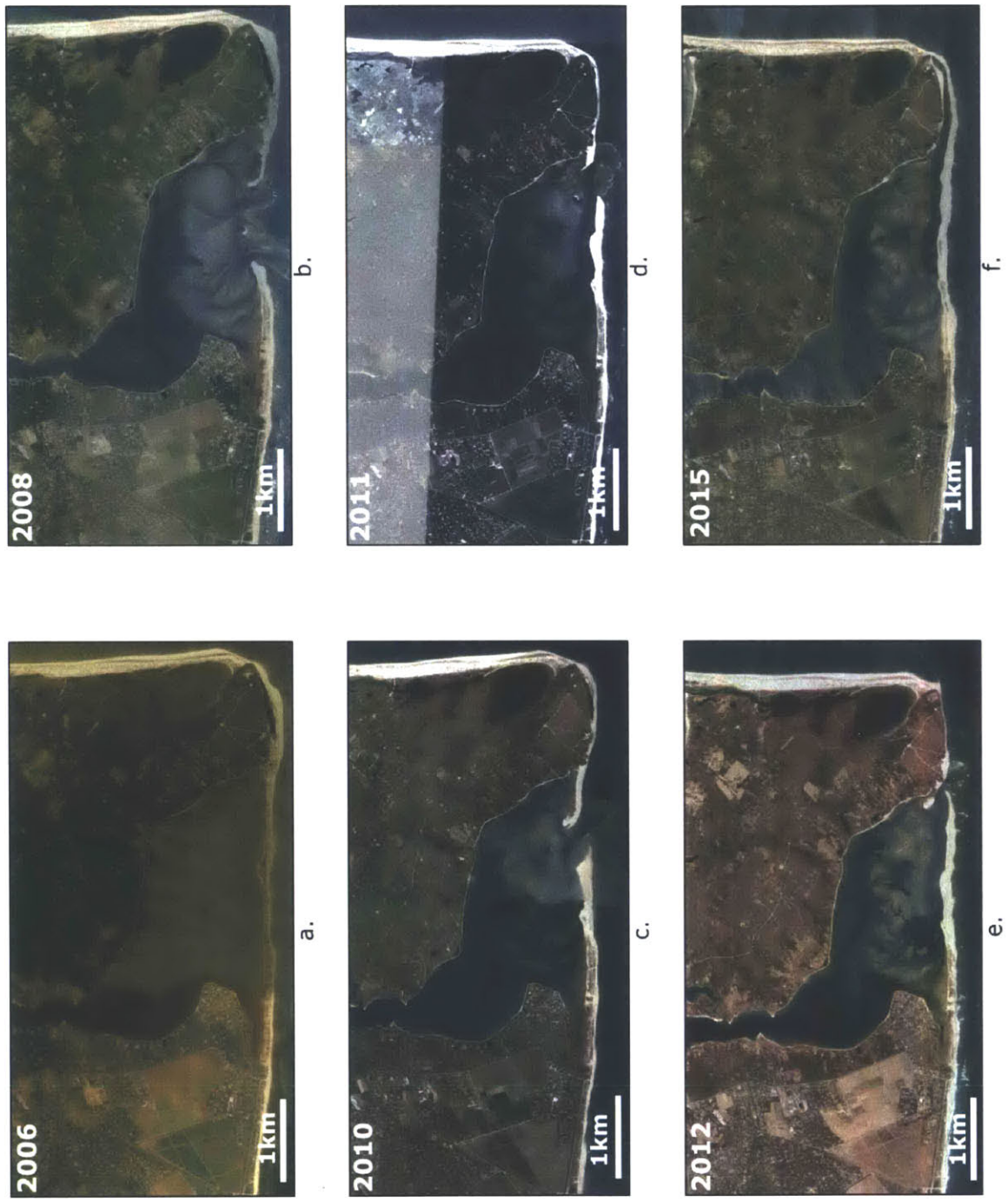

Figure 2.1.2: Chronological evolution of the Katama Inlet between its last closure episode in 2007 (**a**) and today (**f**). From images **b** to **e** there is a yearly migration of the inlet towards the east and Chappaquiddick Island, showing the eight to ten year cyclic breaching/migrating/closing behaviour of the inlet. This figure also shows the erosion of Wasque Point and its increase in angularity reaching a near 90°in 2012 (**e**), up until **f** when the inlet closes and Wasque Point starts smoothing out again. *From GoogleEarth.*

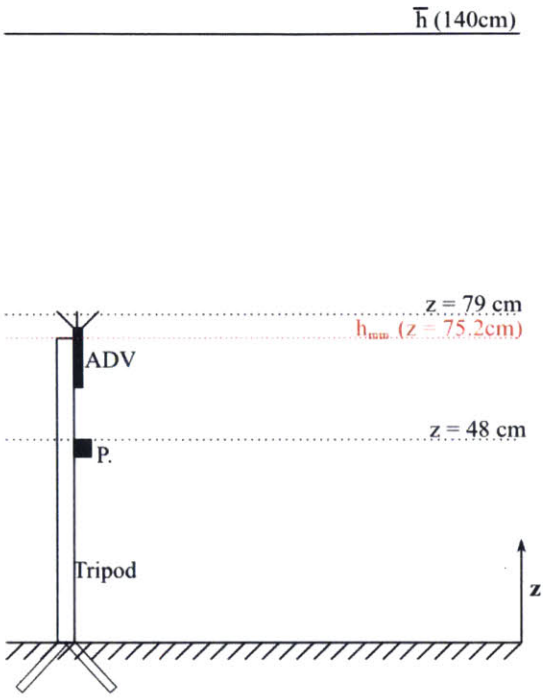

Figure 2.1.3: ADV and pressure sensor setup and position relative to water depth.

the seabed, respectively as shown on Figure 2.1.3, were placed by divers in July 2014. They were mounted on a rigid tripod before the structure was fixed into the sand using a fan shaped-base to lock itself into place. The sensors recorded for about 25 minutes every half hour, starting on the hour, with a sampling frequency of 2 Hz. Sections of this data were then selected, choosing about nine minutes of data (1025 data points) to be processed for every half hour's worth of record and are referred to, in the rest of this project, as "half hour" data. This selection was done in order to facilitate the analysis of the data later on. Bathymetric data was also collected at the time the sensors were deployed and is shown in Figure 2.1.4.This map highlights the contrast between the linear bathymetry along South Beach and the much more complex one offshore of the inlet and around Wasque Point, suggesting how this may contribute to the instability of the flows. Depth corrections were applied to the raw pressure data to make up for the ADV elevation before it was translated into depth (h), significant wave height (H_s) and period ($T_{\eta s}$) using linear wave theory (*Madsen et al.*, 1993). The raw velocities were used to determine wave (U_{ws} and U_{bm}) and current (U_c) velocities and directions (ϕ_w and ϕ_c), as well as the angle difference between the two (ϕ_{wc}) and the wave period T_s. As data was collected

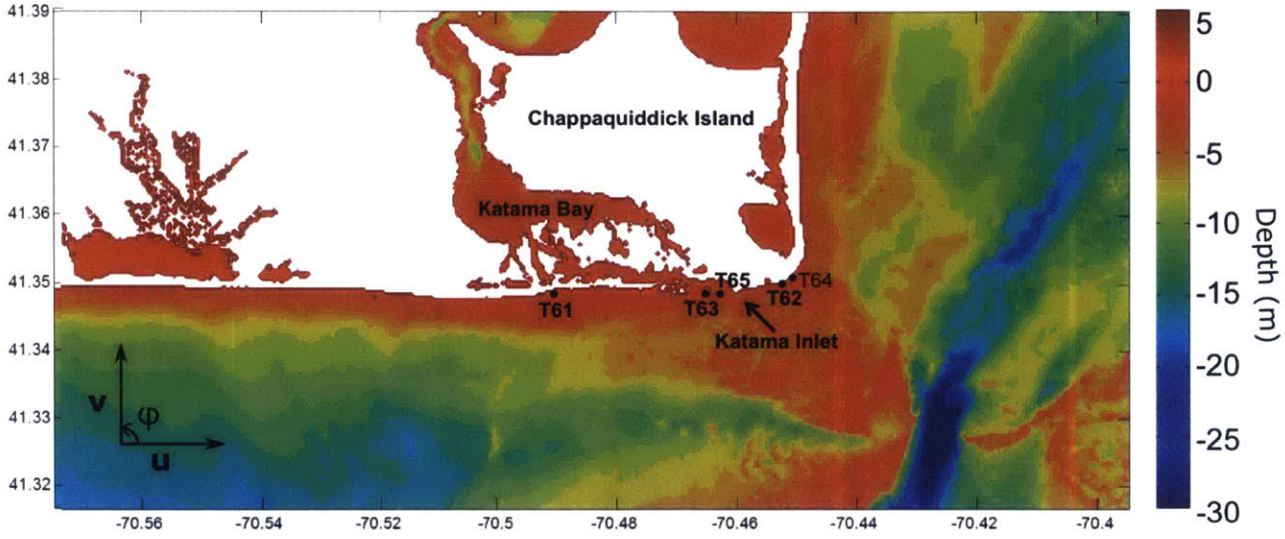

Figure 2.1.4: Bathymetric plot of the study area and position of the sensors relative to contour lines. (From J. Hopkins, (personal communication, May 6, 2016).

over a period of a month, three sub-intervals were studied more specifically to assess the wave and current properties in the area. These were determined from both the available weather data collected in August 2014 on South Beach, Martha's Vineyard, MA (*WHOI*, 2014) to be representative of normal or storm conditions, as well as from the depth to exemplify either the neap tides or the spring tides (Figure 2.1.5). From this data a storm was identified between the 13th and 14th August 2014, with the rest of the survey period considered as normal, i.e. calm wave conditions. The depth plot, which will be further discussed in Section 2.3, was used to show the occurrence of neap tides between the 1st and 7th August, as well as after the 16th August, with a well pronounced spring tide in between. As a result the first studied interval ranged between the 1-3rd August (neap tides), the second one between the 10-12th August (spring tides) and the third between the 13-15th (storm) to sample the high wind period. These intervals are indicated by red dotted lines in Figure 2.1.5. The project was elaborated in two phases: we first looked at the hydrodynamic properties at each sensor, and then evaluated the net sediment transport based on the properties computed in the first stage. Each time T61 was used as the reference location due to its distance from both the inlet and the Muskeget Channel, minimising non linear interactions with currents coming in and out of the inlet (see Figure 2.1.1). In all calculations

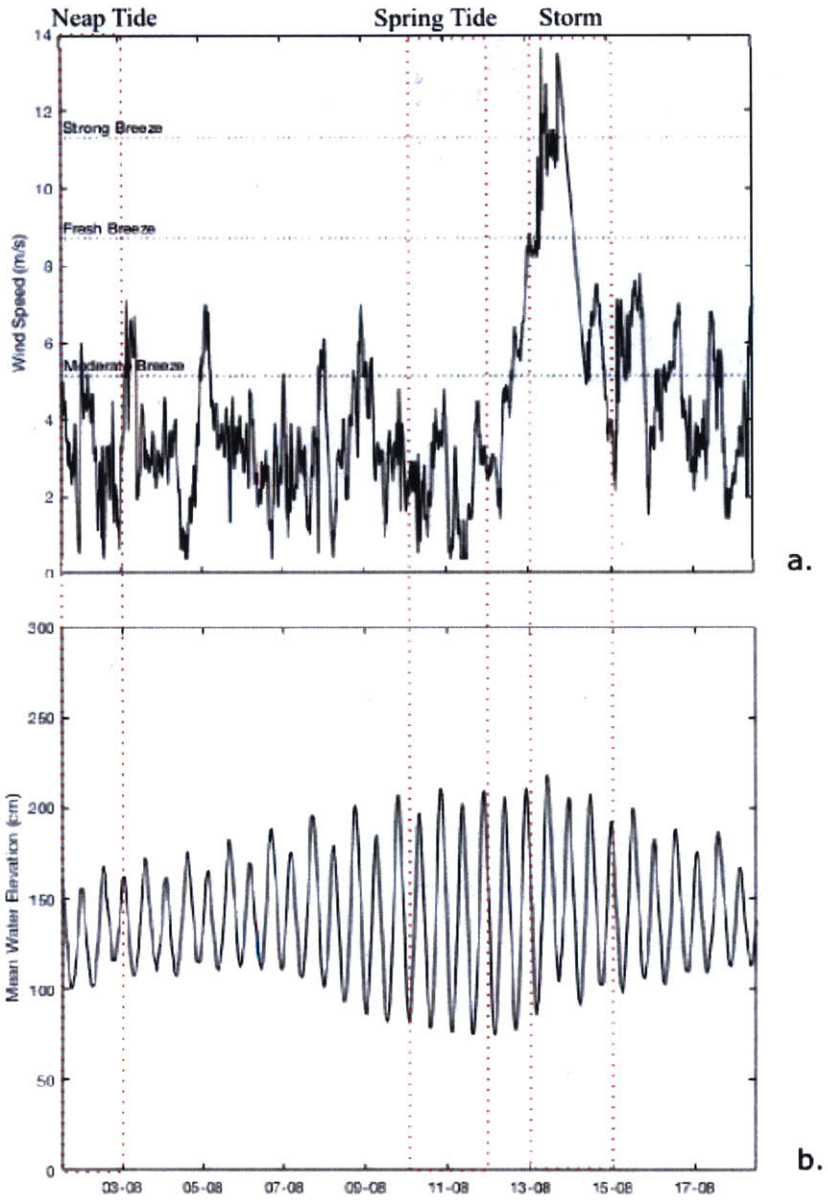

Figure 2.1.5: Wind velocity data collected by the South Beach meteorological mast in 2014 (**a**) and average depth from field measurements (**b**) at T61. The wind velocities are compared to the Beaufort Wind Scale to evaluate the conditions. After data collected by *WHOI* (2014).

angles were measured anti-clockwise, with 0°pointing due East (and 90°corresponding to due North) and velocities were computed using a right handed coordinate system (positive towards the East and the North) as shown on the bathymetry plot (Figure 2.1.4), with $z = 0$ at the bottom for the vertical axis.

2.2 Analysis of the Pressure Data

First the raw pressure data at each half hour was distinguished between average pressures (with $N = 1025$ the number of data points in each half hour of the dataset)

$$\bar{p} = \frac{\sum_1^N p}{N} \tag{1}$$

and wave-induced pressures at each half hour

$$\tilde{p} = p - \bar{p} \tag{2}$$

before being converted into water depth at each half hour, using the density of sea-water $\rho = 1025\ kg/m^3$ and the height above sea level of the pressure sensor, $z_p = 48cm$:

$$h = \frac{\bar{p}}{\rho g} + z_p \tag{3}$$

The long term variation of the water level with tides is shown in Figure 2.1.5 **b.** and has a clear neap/spring tide signature. In the 48 hour time intervals synthesized in Table 2.2.1 (or shown separately in Figure 2.2.1) we can clearly see how this depth varies with the semi-diurnal tidal signal and how it is amplified during the spring tides: the variation in depth δh between the high tides and low tides, the tidal range, doubles between the neap tide and the spring tide. Table 2.2.1 also shows that the stronger tides lead to a 10% increase in the mean water depth whereas the storm has very little impact on this (as confirmed by the similarity in oscillations in the last two plots of Figure 2.2.1).

Linear wave theory was then used to compute wave properties. To justify this basic approach it was initially assumed that the incoming waves were all wind generated and therefore had periods

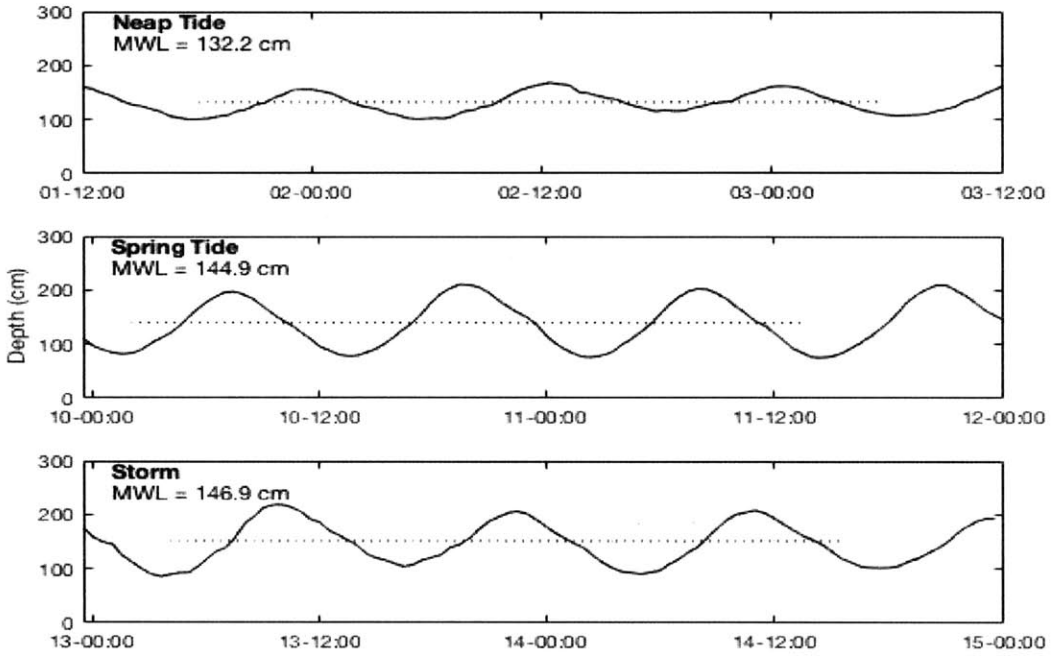

Figure 2.2.1: Depth variation over three distinct 48 hour intervals at T61. The tidal amplitude just about doubles between the neap tide event early August ($a_t = 35cm$) and the spring tide event mid-August ($a_t = 65cm$). The dataset during the storm interval (during the spring tide) shows that the meteorological event has no impact on the mean water level. The dotted lines show the interval over which the depth was compared.

$1second < T < 30seconds$, a small amplitude a and had not yet started breaking. A wave pressure spectrum $S_{\tilde{p}\tilde{p}}$ was hence computed for each half hour data set, and its analysis led to discarding frequencies greater than 0.3 Hz (and hence signals with $T < 3.3seconds$) due to excessive noise and lack of significant data in the higher frequencies (see Figure 2.2.2). We then obtained the surface

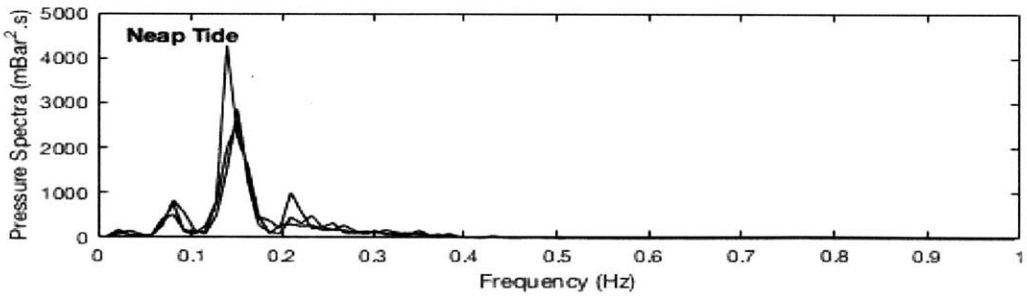

Figure 2.2.2: Pressure spectra at the sensor height $S_{\tilde{p}\tilde{p}}$ for frequencies up to 1 Hz, taken during the neap tide at T61 for several half hours.

spectrum $S_{\eta\eta}$ by translating $S_{\tilde{p}\tilde{p}}$ to the surface using

$$S_{\eta\eta} = \left(\frac{\cosh(kh)}{\cosh(kz_p)\rho g} \right)^2 S_{\tilde{p}\tilde{p}} \tag{4}$$

where the wavenumber k is a function of frequency and was obtained using a Newton-Raphson iteration to solve :

$$\omega^2 = kg \tanh(kh) \tag{5}$$

with ω denotes the angular frequency and h the water depth obtained from Equation 3 for the half hour of data being analysed. Figure 2.2.3 shows good agreement between the surface (at $z = h$) and pressure spectra (at $z = z_p$), with a greater departure in the surface spectra from the pressure spectra at the higher frequencies. This is because as these (and thus k) increase, $cosh(kh) >> cosh(kz_p)$ and so their ratio becomes greater than one. This trend is then furthermore amplified by being squared (see Equation 4), leading to $S_{\eta\eta} > S_{\tilde{p}\tilde{p}}$. The spectral analysis enabled us to obtain the significant wave height H_s at the surface for every half hour of data

$$H_s = 4 \left(\int_0^\infty S_{\eta\eta} d\omega \right)^{1/2} \tag{6}$$

as well as the significant wave amplitude, defined as $a_s = 1/2\ H_s$ and the representative significant wave period,

$$T_{\eta s} = 2\pi \frac{\int_0^\infty S_{\eta\eta} d\omega}{\int_0^\infty \omega S_{\eta\eta} d\omega} \tag{7}$$

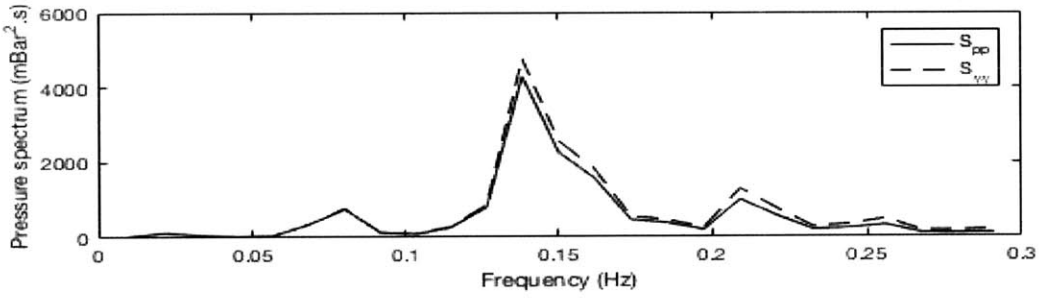

Figure 2.2.3: Pressure spectrum at the sensor height $S_{\tilde{p}\tilde{p}}$ and extrapolated to the surface $S_{\eta\eta}$ for T61.

with $\omega_s = \frac{2\pi}{T_{\eta s}}$ the centroid frequency. The results presented in Figure 2.2.4 and summarized in

Table 2.2.1: Wave and current characteristics derived from the pressure data for each studied interval. The δ terms correspond to a representative difference between the highest and lowest values of each characteristic divided by two, as an approximation for the amplitude of the variation due to the tides.

	Neap Tide	**Spring Tide**	**Storm**
date	1-3rd August	10-12th August	13th-15th August
$\mathbf{h_{mean}}$ **(cm)**	132.2	144.9	146.9
δh (cm)	31.0	61.5	58.0
$\mathbf{a_s}$ **(cm)**	21.6	15.5	38.2
$\mathbf{\delta a_s}$ **(cm)**	4.6	5.5	13.3
$\mathbf{T_{\eta s}}$ **(s)**	6.3	8.9	6.5
$\mathbf{\delta T_{\eta s}}$ **(s)**	0.25	1.50	0.55

Table 2.2.1 confirm the legitimacy of using linear wave theory here, as $T_{\eta s}$ is within the specified interval and give us a characteristic value of $T_{\eta s} = 6.3 \pm 0.25s$ and $17cm < a_s < 26cm$ for the neap tide conditions. The mean amplitude of each characteristic's variation with the tides δ is shown as well in Table 2.2.1 to highlight not only the effect of the spring tide on this variation, but also to give the reader a feeling for magnitude of this variation. The three different scenarios however show different interactions between the tides and waves over a few tidal cycles. During the neap tides and normal meteorological conditions, when the tidal and wave amplitudes are relatively small, the waves are independent of the tidal oscillation and the amplitude remains fairly constant. As the tidal amplitude increases however in the two spring tide intervals, the wave amplitude starts oscillating in phase with the tides, with higher amplitudes corresponding to larger water depths. The storm adds on the effect of increasing the mean wave amplitude by over 50% (Table 2.2.1). The period is also shown to increase very slightly due to the storm, but more surprisingly, it increases dramatically between the neap and spring tides (by 40%), and it oscillates with the tides during the spring tide with a relatively large oscillation amplitude $\delta T_{\eta s}$. When comparing this with the surface spectrum at low and high tide (see Figure 2.2.5) we can see that the main frequency peaks are slightly offset

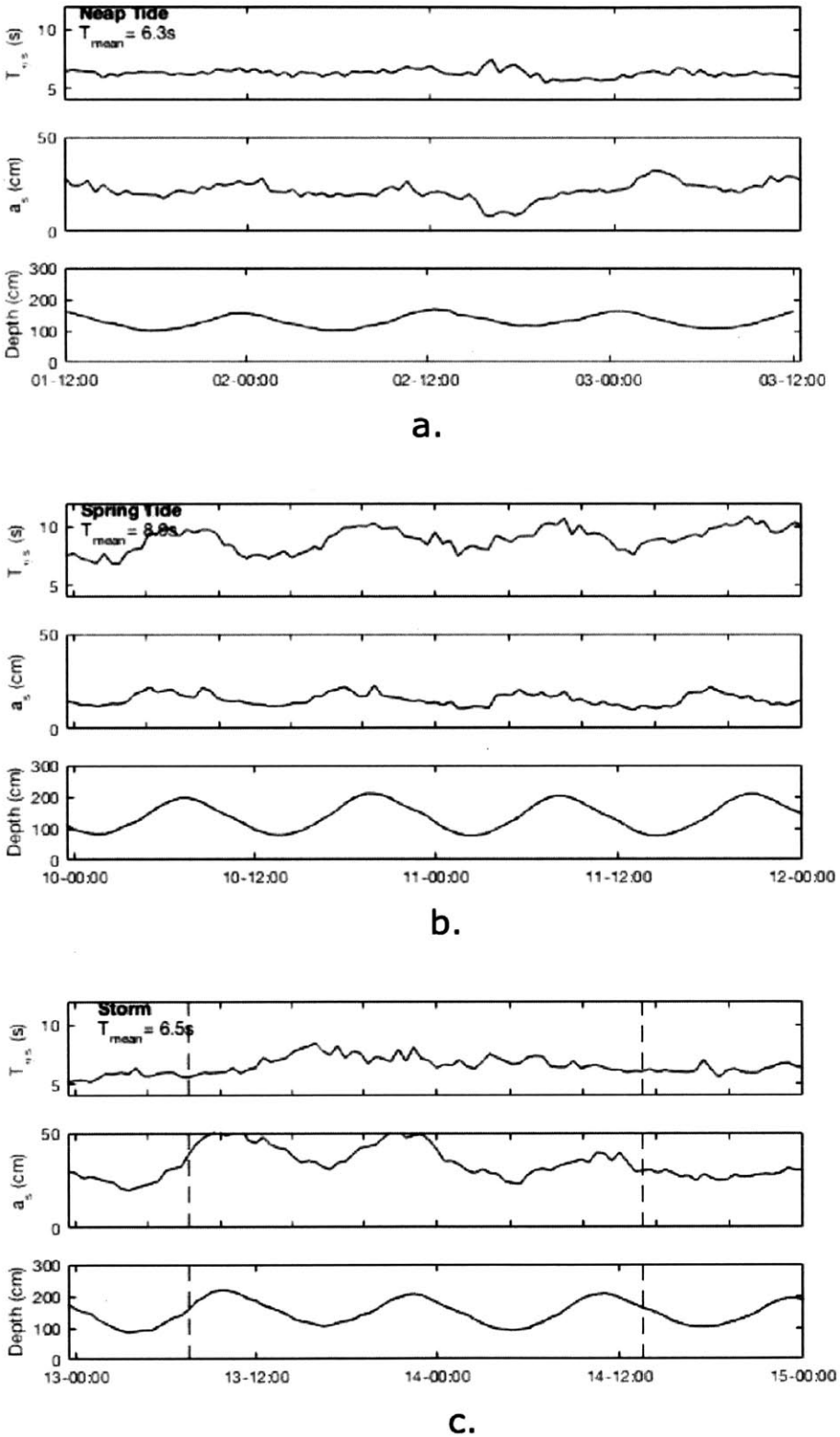

Figure 2.2.4: Wave period $T_{\eta s}$ and significant wave height H_s obtained from the pressure data at T61 during the neap tide, spring tide and storm events.

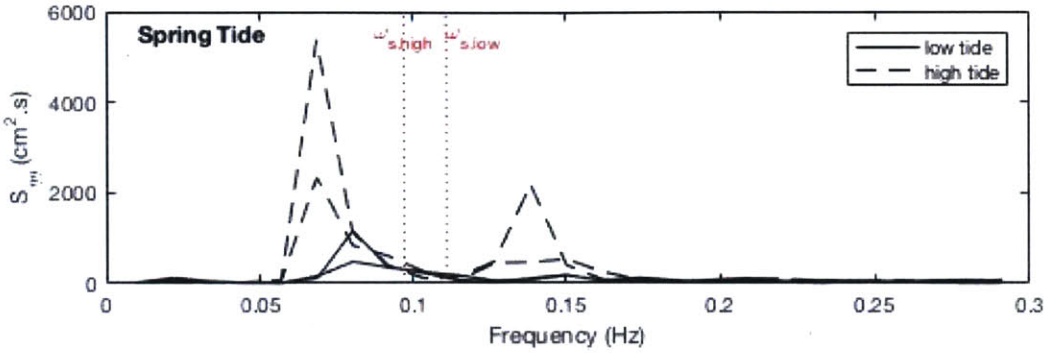

Figure 2.2.5: Surface spectra at low and high tide highlighting the shift in the frequency of the highest peaks for each tide. At low tide, $\omega = 0.078Hz$ and at high tide $\omega = 0.07Hz$. As a direct consequence of this ω_s switches with the tides too.

between the two stages, leading to the centroid frequency ω_s flipping back and forth between two values, and this is what translates into the period oscillation. No physical explanation for this shift has been found so far however and as a consequence when this data is used later on in the project, the oscillation is ignored and the $T_{\eta s,spring,mean} = 8.9s$ is assumed as the representative period for that interval. To further understand the correlation between the waves and the tides during the spring tides, we computed the orbital wave velocity amplitude ($\widetilde{U_p}$) to identify any similar trends. By plotting it as a function of depth z we were able to assess the vertical decay in velocity (very little would be expected as the study is performed in about two meter depth (Figure 2.1.4), which is considered as a shallow water environment). The value computed at the bottom U_{bm} could be compared later to the wave velocity amplitude obtained from the velocity data to measure the accuracy of obtaining this value from pressure data. It is expected the velocities obtained from the pressure would overestimate those measured by the ADV: having no directional information so far, the computations assumed unidirectional waves and hence focused all the wave energy onto a single direction. In reality the waves would never all have perfectly identical directions.

In order to compute these orbital wave velocities we converted the surface spectrum $S_{\eta\eta}$ into velocity spectra, both at the velocity sensor height ($z_u = 79$ cm) and at the bottom ($z = 0$) using

$$S_{\tilde{u}\tilde{u}}(z = z_u) = S_{\eta\eta}\left(\omega \frac{cosh(kz_u)}{sinh(kh)}\right)^2 \tag{8}$$

and

$$S_{\tilde{u}\tilde{u}}(z=0) = S_{\eta\eta}\left(\omega\frac{1}{sinh(kh)}\right)^2 \tag{9}$$

The velocity amplitude was then obtained in the same fashion as in Equation 6 with

$$U_p = 2\left(\int_0^\infty S_{\tilde{u}\tilde{u}}d\omega\right)^{1/2} \tag{10}$$

Another way of confirming these results was by bulk calculating the orbital velocities (U_b), assuming representative conditions for each half hour using the centroid frequency ω_s, the associated wavenumber k_s and the wave amplitude a_s:

$$U_b = a_s\omega_s\frac{cosh(k_s z)}{sinh(k_s h)} \tag{11}$$

with $z = z_u$ and $z = 0$ to be able to directly compare these results to those using the method described in Equations 8 and 10. The results are presented in Table 2.2.2 which also compares them to the values obtained from the velocity data, and discussed later. The results plotted in Figure 2.2.6

Table 2.2.2: Wave orbital velocities computed from the pressure data both at $z = z_u$ and at $z = 0$, and wave velocity as measured by the ADV sensors at $z = z_u$.

(cm/s)	Neap Tide	Spring Tide	Storm
U_p ($z = z_u$)	57.9	41.6	91.7
U_p ($z = 0$)	56.2	40.8	89.5
U_b ($z = z_u$)	58.1	41.7	92.6
U_b ($z = 0$)	56.6	41.1	91.3
U_{wc} ($z = z_u$)	52.3	39	87.2

and tabulated in Table 2.2.2 show a maximum 3% decrease in the orbital velocity amplitude between $z_u = 79cm$ and the bottom, regardless of whether representative conditions for each half hour, or the surface spectrum were used, allowing us to neglect the decay and so to use the velocity sensor height computed velocities in the sediment transport calculations. Furthermore, the difference between these two methods to get orbital velocity present less than 1% difference, showing how in these shallow

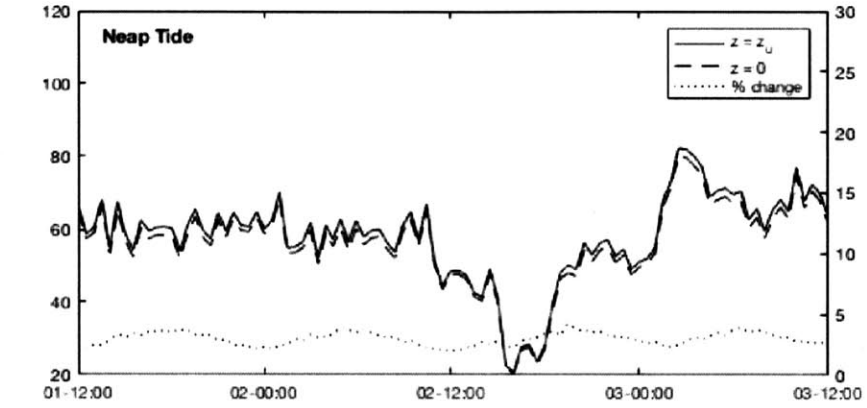

a.

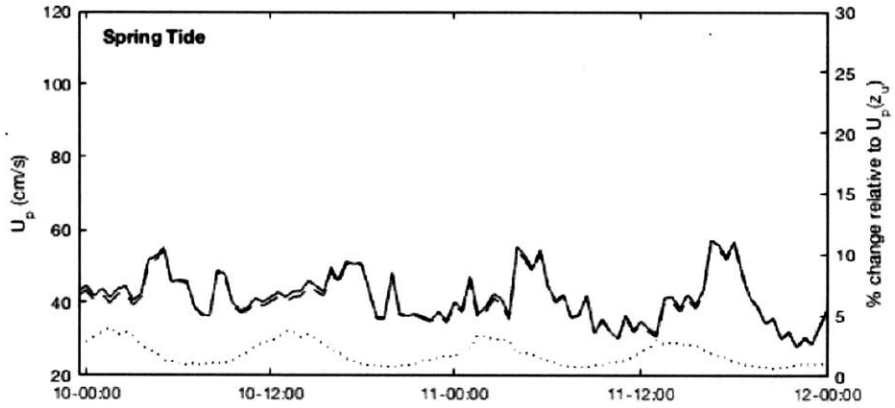

b.

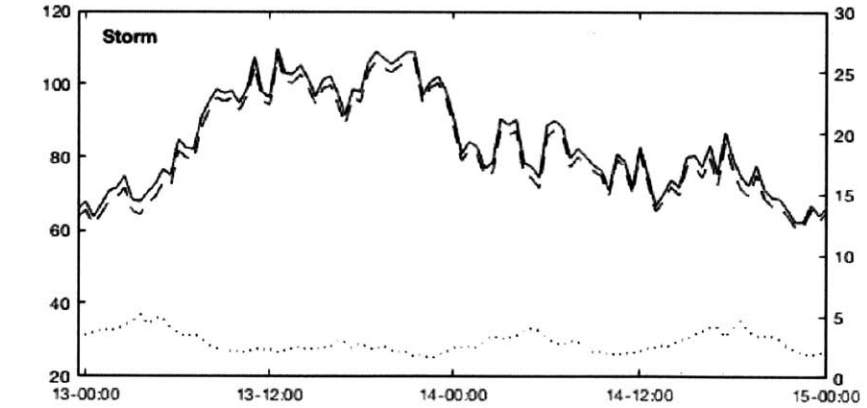

c.

Figure 2.2.6: Orbital wave velocity for T61, during the neap tide, spring tide and storm events. As this is obtained from the pressure signal, the velocity profile follows the same pattern as the amplitude one.

water environments, the simplification of bulking all waves within each half hour is a sound approximation. Finally the increase in wave velocity from the normal conditions (Table 2.2.2) to the storm by a factor of two, correlates well with the increase in wave amplitude observed in Table 2.2.1 (as expected as U_p is related to a_s).

This analysis has so far showed that in normal conditions combined with weak neap tides, the waves remain constant with time and their characteristic properties ($T_{\eta s}$ and a_s) therefore depend very little on the current conditions. During the spring tides however, a_s, h and U_p oscillate in phase with each other. We therefore have conditions in which, at high tide (greater depth h), the wave amplitude is greater than at low tide. The effect of the storm, added on to the greater spring tides, seems to amplify this increase even more.

Finally, with all the the half hour characteristics of the pressure data in hand, we then looked into the longer term behaviour of the waves for further confirmation of their correlation to currents. We performed a spectral analysis of these slower (one point per half hour) varying attributes using variations in h for the currents, and in H_s for the waves. Spectra were thus obtained from,

$$\eta_T = h - \bar{h} \tag{12}$$

and,

$$\eta_{H_s} = H_s - \bar{H}_s \tag{13}$$

These slow-varying spectra (Figure 2.2.7) show that the long term variation of the surface wave height has the same oscillating frequency as the semi-diurnal M_2 tide, with the first harmonic of the slow surface wave height variation matching that of the depth, for a tidal period $T_t = 1/0.08 = 12.5hours$. From this we can infer that the tides (described by the slow variation in depth) and the waves (described by the slow variation in surface wave height) must have some effect on each other, and hence should not be seperated for the sediment transport analysis as this would lead to ignoring an entire aspect of the sediment perturbing motions. The presence of a diurnal signal observed especially in the quiet conditions with $T_{O_1} = 25hours$, as well as the shallow water overtides M_4 and M_6 during the spring tides (with $T_{M_4} = 6.25hours$ and $T_{M_6} = 4.16hours$) in the depth variation highlights the importance

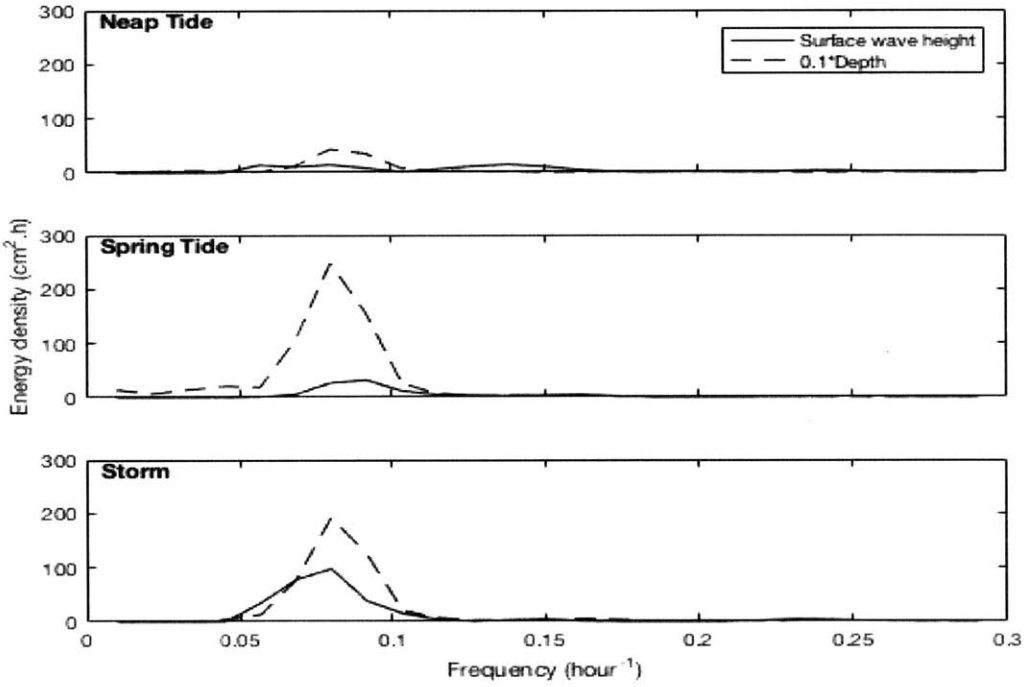

Figure 2.2.7: Slow variation of the surface wave height and depth at T61, for the selected three 48 hour intervals.

of the tides on the hydrodynamics of this area. However, these results show, again, a great difference in the strength of this correlation depending on the tidal and meteorological conditions: during the neap tide, the first harmonic of the wave surface height is much smaller than that of the tidal surface height. The difference in energy density between the two decreases with stronger conditions, and is at its lowest in the storm conditions (which are combined with the spring tide). This amplification correlates well with the similar increase in wave amplitude (see Figure 2.2.4) and suggests that the relationship between wave height variation and tides does exist at all levels of energy density (but is more easily observable in rougher environments), and hence highlights the importance of including it in sediment transport calculations.

2.3 Analysis of the Velocity Data

The velocity data was, similarly to the pressure data, first decomposed into current and wave at each half hour, with the average velocity for the half hour representative of the current conditions over that

time, and the time-varying velocities within the half hour representative of the wave conditions, i.e.

$$(\bar{u}, \bar{v}) = \frac{\sum_1^N (u, v)}{N} \tag{14}$$

and

$$(\tilde{u}, \tilde{v}) = (u - \bar{u}, v - \bar{v}) \tag{15}$$

The current direction was then assessed as

$$\phi_c = \tan^{-1}(\frac{\bar{v}}{\bar{u}}) \tag{16}$$

and the projected current velocity U_c was defined as

$$U_c = \bar{u}cos(\phi_c) + \bar{v}sin(\phi_c) \tag{17}$$

The coordinate system used in this analysis is shown in Figure 2.1.4, defining **u** pointing towards the East, and **v** as pointing towards the North. Starting with the current analysis, Figure 2.3.1 shows the currents' strong semi-diurnal tidal component by plotting the slow-varying current energy distribution (from U_c) over the analysed frequency spectrum. Similarly to the results of the slow-varying depth presented in Figure 2.2.7, this energy distribution shows a distinct peak at a frequency of $0.08hour^{-1}$, or a period of $12.5hours$ which corresponds to the M_2 semi-diurnal tide. Two other small peaks marking the M_4 and M_6 spring tides are also observed, confirming the results obtained from the pressure data that the currents are essentially controlled by the tides.

The intensity of the tide in each direction is also highly asymmetric: the velocities U_c, detailed in Table 2.3.1 are skewed towards the positive (Figures 2.3.2 to 2.3.4) with eastward (positive and corresponding to $\phi_c = 360°$) velocities greater than the westward (negative and corresponding to $\phi_c = 180°$) ones by $30 - 170\%$, indicating much stronger tides towards the east than towards the west. $U_{westward}$ represents the minimum(or most negative) velocities whereas $U_{eastward}$ corresponds to the highest and most positive values. This skewness increases with the strength of the tides, and is hence even more noticeable during the spring tides ("spring tide" and "storm" intervals) than it is

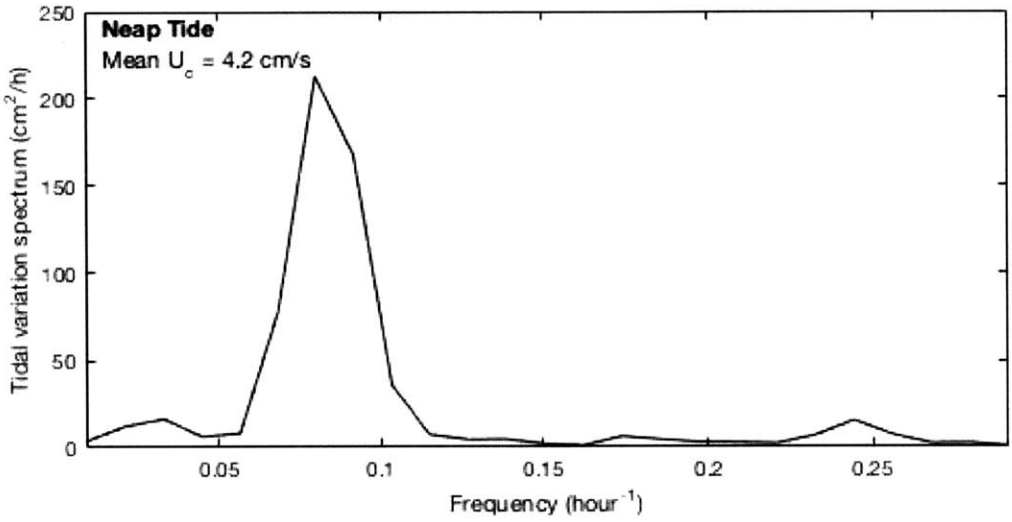

Figure 2.3.1: Spectra of the current velocity, emphasizing the predominance of the semi-diurnal tide relative to the total current energy distribution.

during the neap tides. This is in agreement with the current pattern observed in the larger geographic area, as discussed in section 2.1.1, and comforts us about the existence of a "shadow" zone created by the outgoing tide, flowing out of the Vineyard Sound through Muskeget Channel. The comparison with the depth time series shows that during the neap tide (Figure 2.3.2), the spring tide (Figure 2.3.3) and the storm interval (Figure 2.3.4), the high current velocities always correspond to the high water depths, and hence that the two are essentially in phase, with the shift between the peaks (highlighted by dotted red lines in the Figures) is marginal.

Table 2.3.1: Current velocities at each time interval at T61, as obtained from the velocity data.

(cm/s)	Neap Tide	Spring Tide	Storm
$U_{c,mean}$	4.2	9.1	11.7
$U_{c,eastward}$	24.3	38.2	35.0
$U_{c,westward}$	-19.1	-22.8	-11.9

As both mid-August intervals are dominated by the spring tides it was expected that the current conditions should be similar between the two, which is indeed observed with the storm interval show-

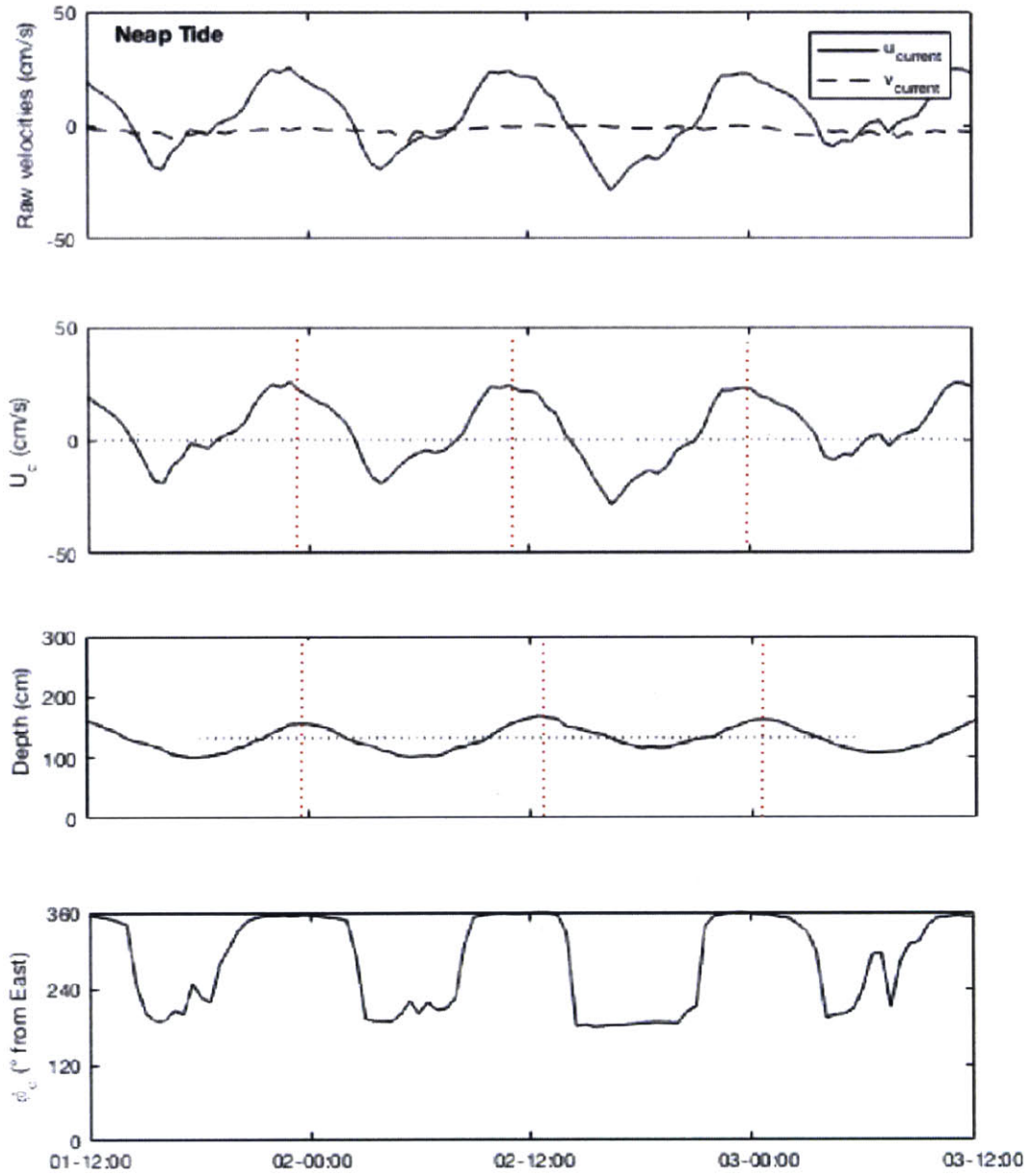

Figure 2.3.2: Current characteristics obtained from the velocity data for T61 during the neap tides compared to the depth. $u_{current}$ and $v_{current}$ correspond to $\bar{u}$ and $\bar{v}$ in the text respectively.

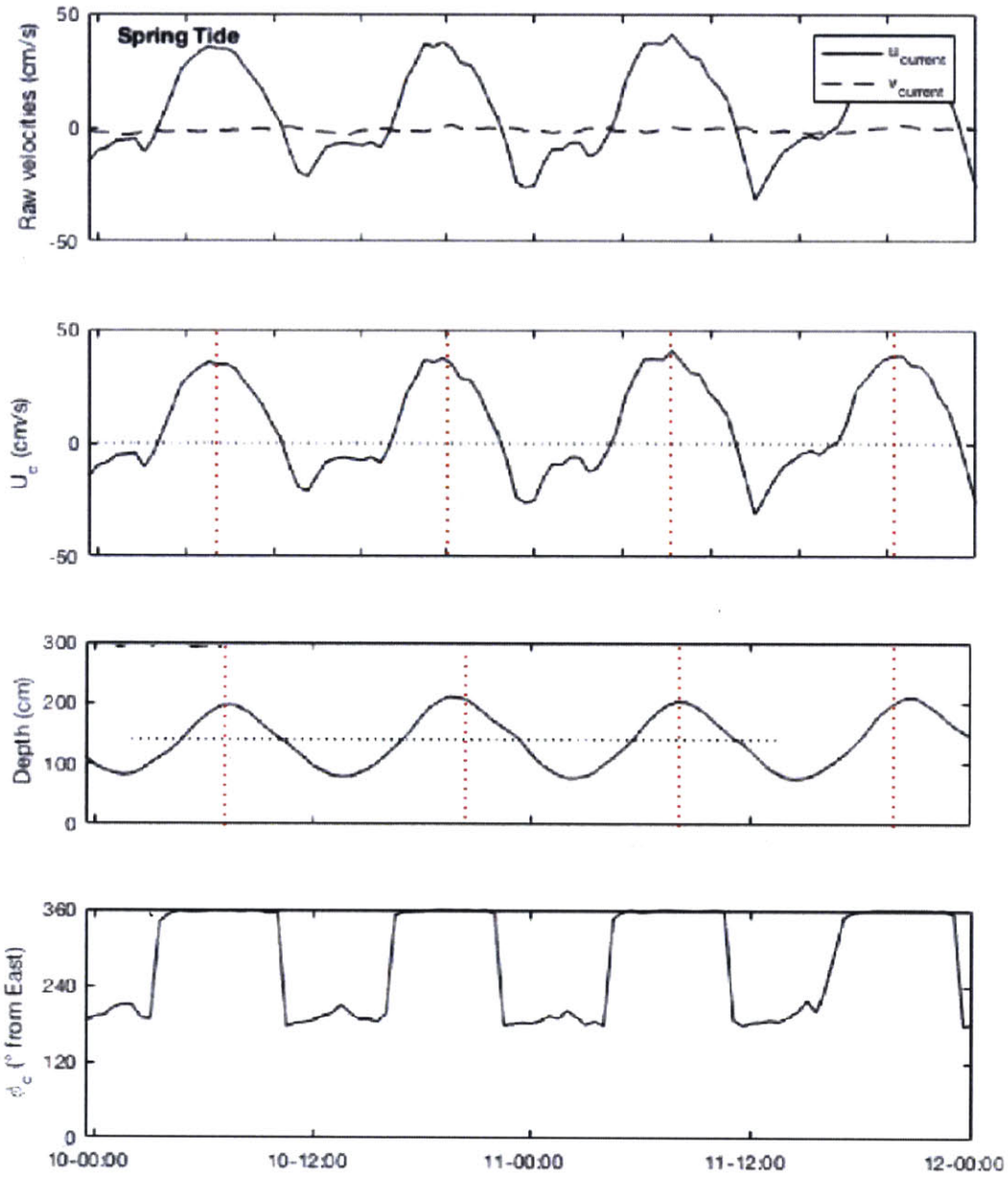

Figure 2.3.3: Current characteristics obtained from the velocity data for T61 during the spring tides compared to the depth ($u_{current}$ and $v_{current}$ correspond to $\bar{u}$ and $\bar{v}$ in the text respectively).

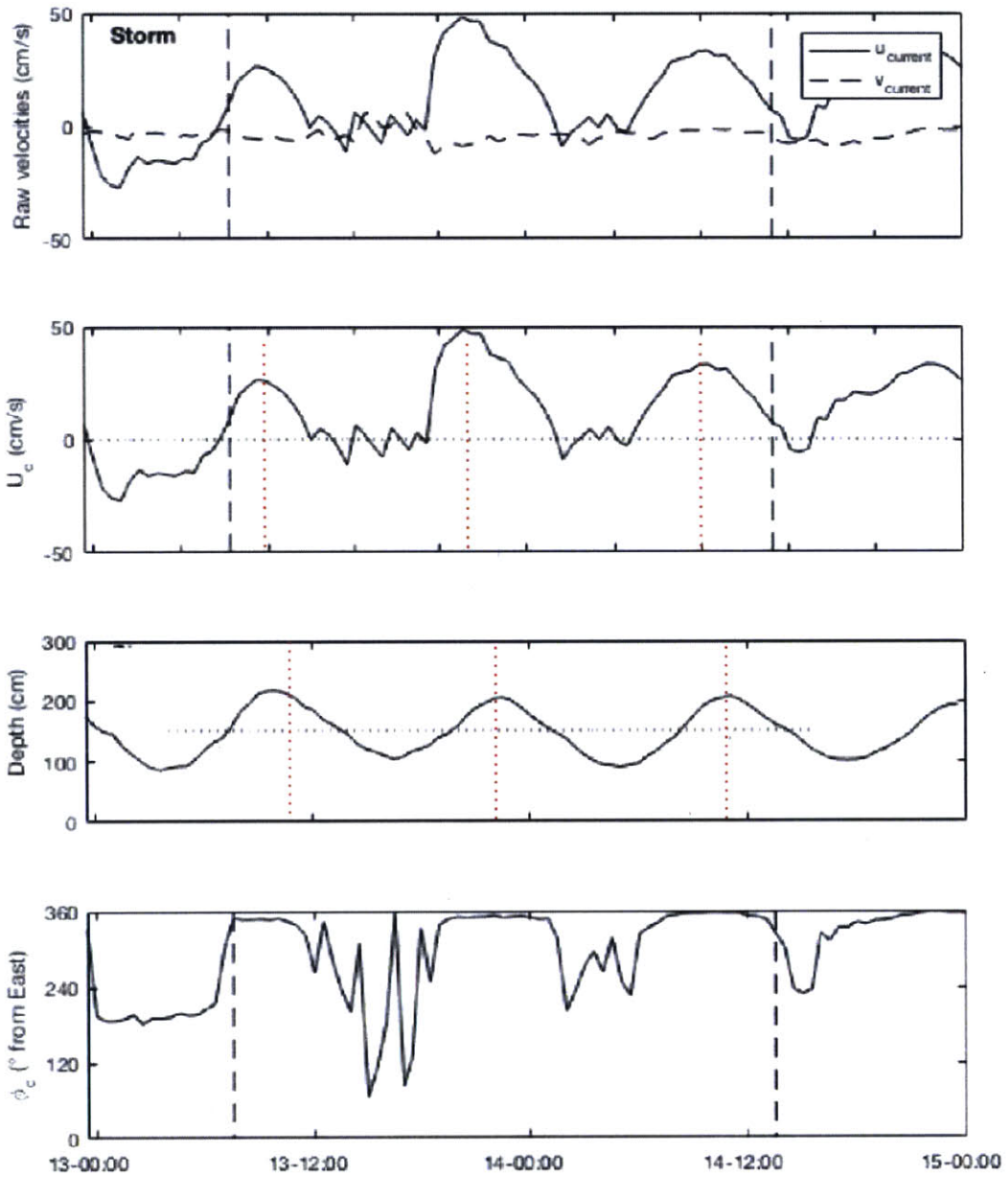

Figure 2.3.4: Current characteristics obtained from the velocity data for T61 during the storm compared to depth ($u_{current}$ and $v_{current}$ correspond to $\bar{u}$ and $\bar{v}$ in the text respectively). Some of the data presents some unusual variations, especially where we would be expecting negative velocities (around 1400-1500 on the 13th, and 0100-0200 on the 14th) and $\phi_c \approx 180°$. The noise in the raw velocity measurements is what leads to the odd direction values, and an explanation regarding this noise will be explained in Section 2.4. The vertical dashed lines delimit the storm interval.

ing $U_{c,max}$ within 8% of the spring interval. The skewness seems somewhat enhanced however during that interval, as $\overline{U_c, storm}$ is 30% greater than that of the spring tide. This difference could be explained by the somewhat unusual "peaks" in the data (Figure 2.3.8 where the current velocity would have been expected to be stable and negative (around the 13th at 1300-1400 or around the 14th at 1400-1500) Explanations as to these peaks will be detailed in Section 2.4, but they were ignored in the rest of the analysis, with the currents assumed to behave with a 12.5 hour period throughout each time interval.

For the wave signal analysis, total wave velocities and directions were first estimated using basic geometry for every record within each half hour:

$$\widetilde{U} = \sqrt{\tilde{u}^2 + \tilde{v}^2} \tag{18}$$

$$\phi = \tan^{-1}(\frac{\tilde{v}}{\tilde{u}}) \tag{19}$$

These enabled us to determine a dominant wave direction ϕ_w for each half hour record using the energy distribution of the wave velocities from the definition of the variance,

$$\sigma_u{}^2(\phi) = \sum_n \widetilde{U}^2 \tag{20}$$

with n the number of values falling within a directional 1° bin around ϕ. The variance was then plotted against these wave directions and the dominant wave direction was determined from the centroid velocity variance for the highest peak (centred around 90° and corresponding to the bulk of the energy carried by the wave, heading onshore),

$$\phi_w = \frac{\sum_{\phi=0}^{180} \sigma_u^2(\phi)\phi}{\sum_{\phi=0}^{180} \sigma_u^2(\phi)} \tag{21}$$

as shown in Figure 2.3.5, with the second peak (centred around 270°) representing the wave motion under the trough (and hence heading offshore). To correct for short time scale variations in the wave direction (within each half hour), the wave velocities were all projected onto the dominant wave direction at that time, enabling a more accurate analysis of the velocity data later on (to correct for the

fact that most calculations will be based on the magnitudes of the velocity vectors, hence not taking into account direction). Using trigonometry, the projected wave velocity became for each half-hour:

$$\widetilde{U_w} = \tilde{u}\cos(\phi_w) + \tilde{v}\sin(\phi_w) \tag{22}$$

As when analysing the pressure data, a spectral analysis of the wave velocity was performed with data associated with $\omega > 0.3Hz$ discarded (for the same reasons as previously). From the velocity spectrum we then obtained the significant wave velocity amplitude:

$$U_{ws} = 2\left[\int_0^\infty S_{\widetilde{U_w}\widetilde{U_w}}\, d\omega\right]^{1/2} \tag{23}$$

and the significant wave period:

$$T_s = 2\pi \frac{\int_0^\infty S_{\widetilde{U_w}\widetilde{U_w}}\, d\omega}{\int_0^\infty \omega S_{\widetilde{U_w}\widetilde{U_w}}\, d\omega} \tag{24}$$

The results for each interval one shown in Figures 2.3.6, 2.3.7 and 2.3.8, and summarized in Table 2.3.2, highlight the change in wave behaviour depending on the conditions. Whereas the dominant wave direction remains constant with time across all three time intervals ($\phi_w = 87° \pm 1°$ and the

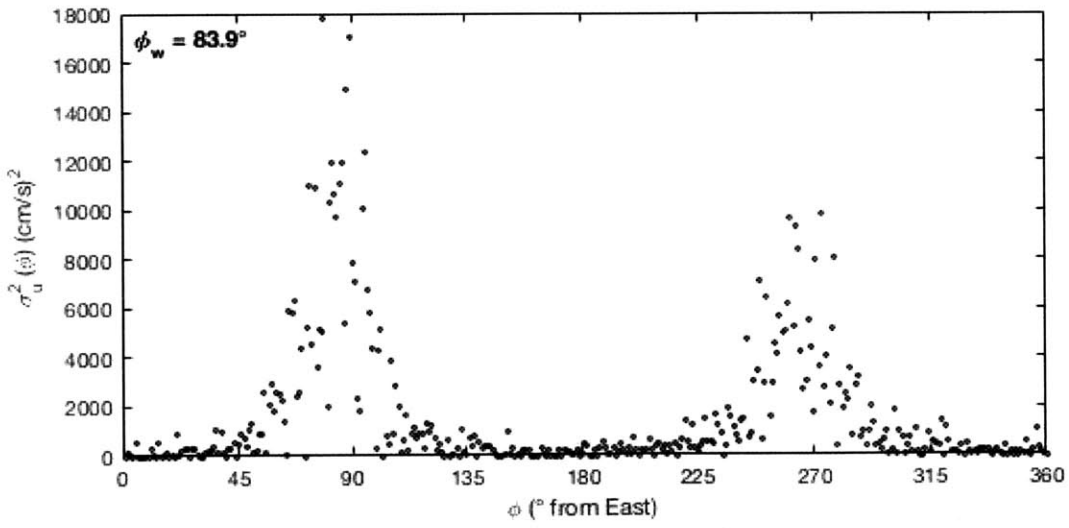

Figure 2.3.5: Example variance plot of the wave velocity at T61 used to determine the dominant wave direction for each half hour.

Table 2.3.2: Wave characteristics at each time interval as well as their representative tidal variation amplitude δ.

	Neap Tide	Spring Tide	Storm
$U_{ws,\,mean}$ (cm/s)	52.30	39.10	87.20
δU_{ws} (cm/s)	8.1	13.9	11.7
T_s (s)	6.1	8.9	6.5
δT_s (s)	0	0.95	0.6

raw velocities $\tilde{u}$ and $\tilde{v}$ show a net asymmetry, with a bias towards the north-south component), the wave velocity amplitude and the period are much more easily affected: in quiet, low tidal amplitude conditions, the wave characteristics remain constant, suggesting no direct interference between the waves and the currents then. As the tidal amplitude increases, during the spring tides, the velocity becomes much more related to the fluctuations in the water level (when comparing Figure 2.3.7 with Figure 2.2.1) as they are high when the water level is high and their tidal variation amplitude δU_c increases with the increased tides. The period also seems to increase and shift with the tides, although this effect will be neglected, like from the pressure observations, due to a lack of physical explanation for this. Finally as the wind speed picks up, the wave velocity increases dramatically, mimicked by a smaller, yet significant increase in the wave period over that same time. The behaviour of all the wave characteristics computed from the velocity data correlate extremely well with the data obtained from the pressure, giving satisfaction that even the unexpected lower wave velocities during the spring tide are not artefacts. Indeed, as shown in Table 2.2.2, the velocities computed from the pressure only overestimate the velocity obtained from the velocity records by 10%, and this is due to the assumed unidirectionality of the waves (whereas the velocity data measures them over the entire range, and takes the variability into account through the projected velocities, Equation 22). The wave period also have excellent agreement between the two measuring techniques, with Table 2.5.1 showing a maximum of 3% variation between the two datasets.

As velocity data isn't always available (or even reliable, see Section 2.4), the good correlation between pressure and velocity measurements is a good justification to using velocities and periods obtained from the pressure data without over-approximating the problem, or introducing much error

into it.

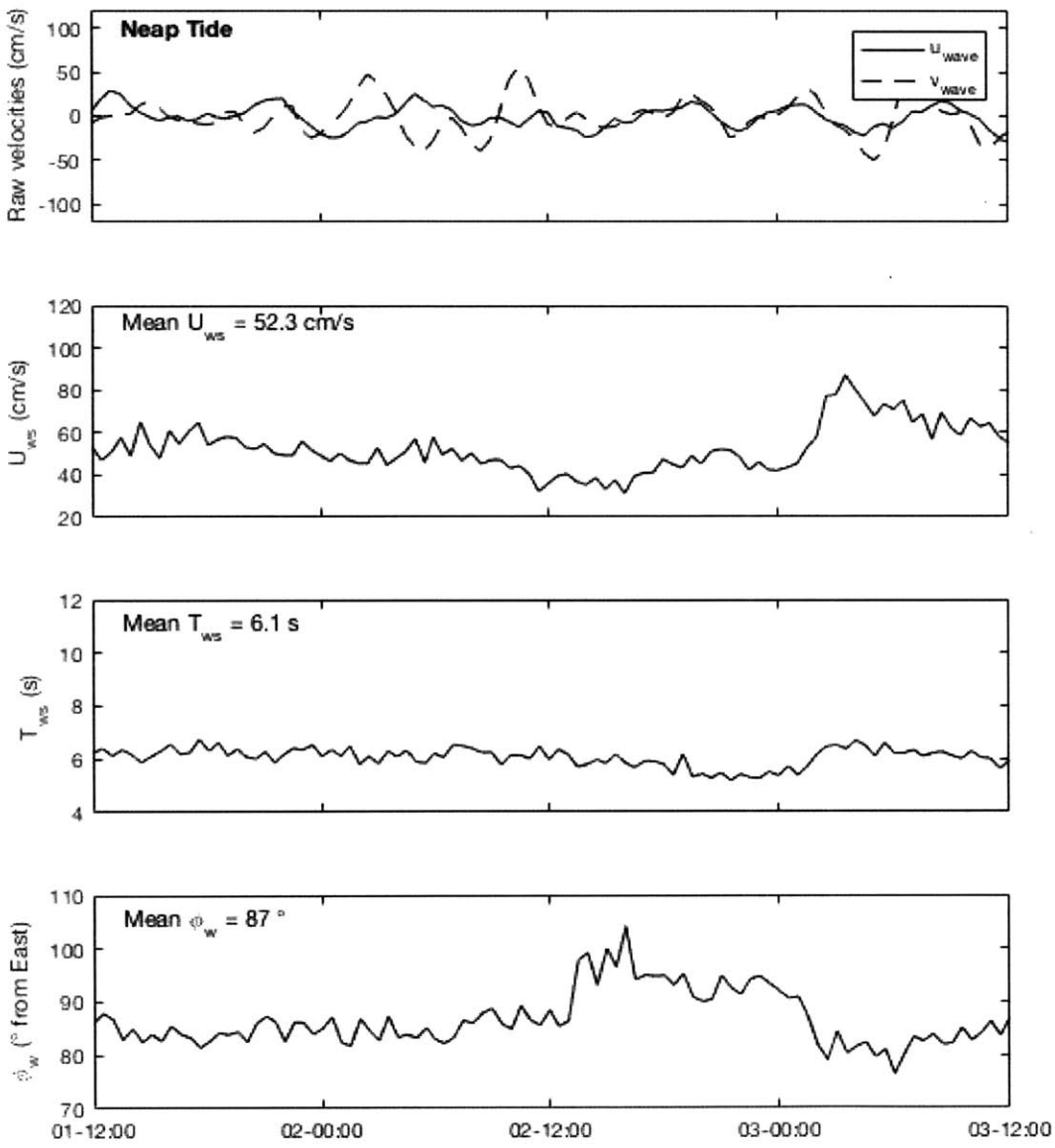

Figure 2.3.6: Characteristic wave properties for T61 during the neap tide interval. u_{wave} and v_{wave} on the plot correspond to $\tilde{u}$ and $\tilde{v}$ respectively in the text.

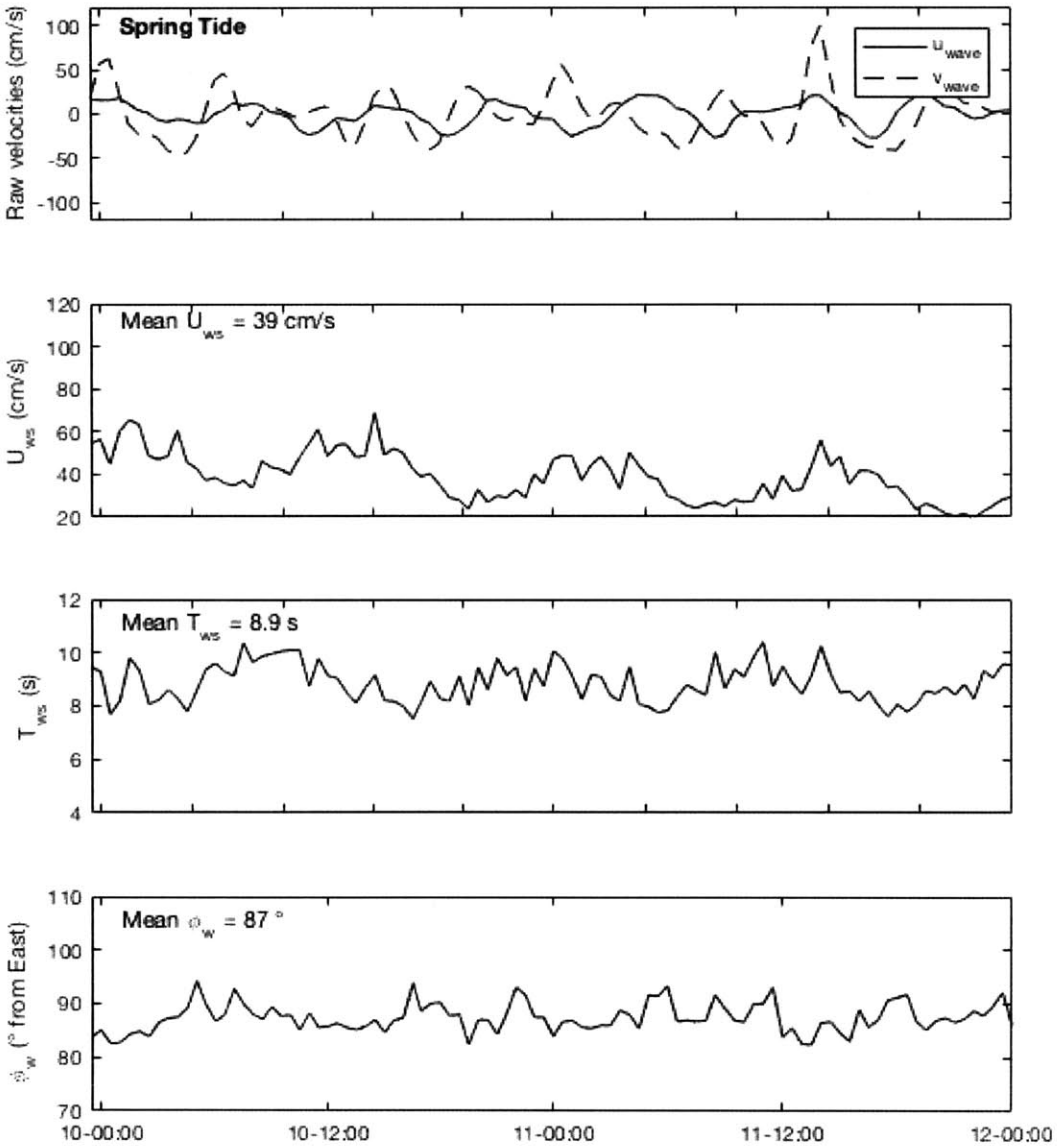

Figure 2.3.7: Characteristic wave properties for T61 during the spring tide interval. u_{wave} and v_{wave} on the plot correspond to $\tilde{u}$ and $\tilde{v}$ respectively in the text.

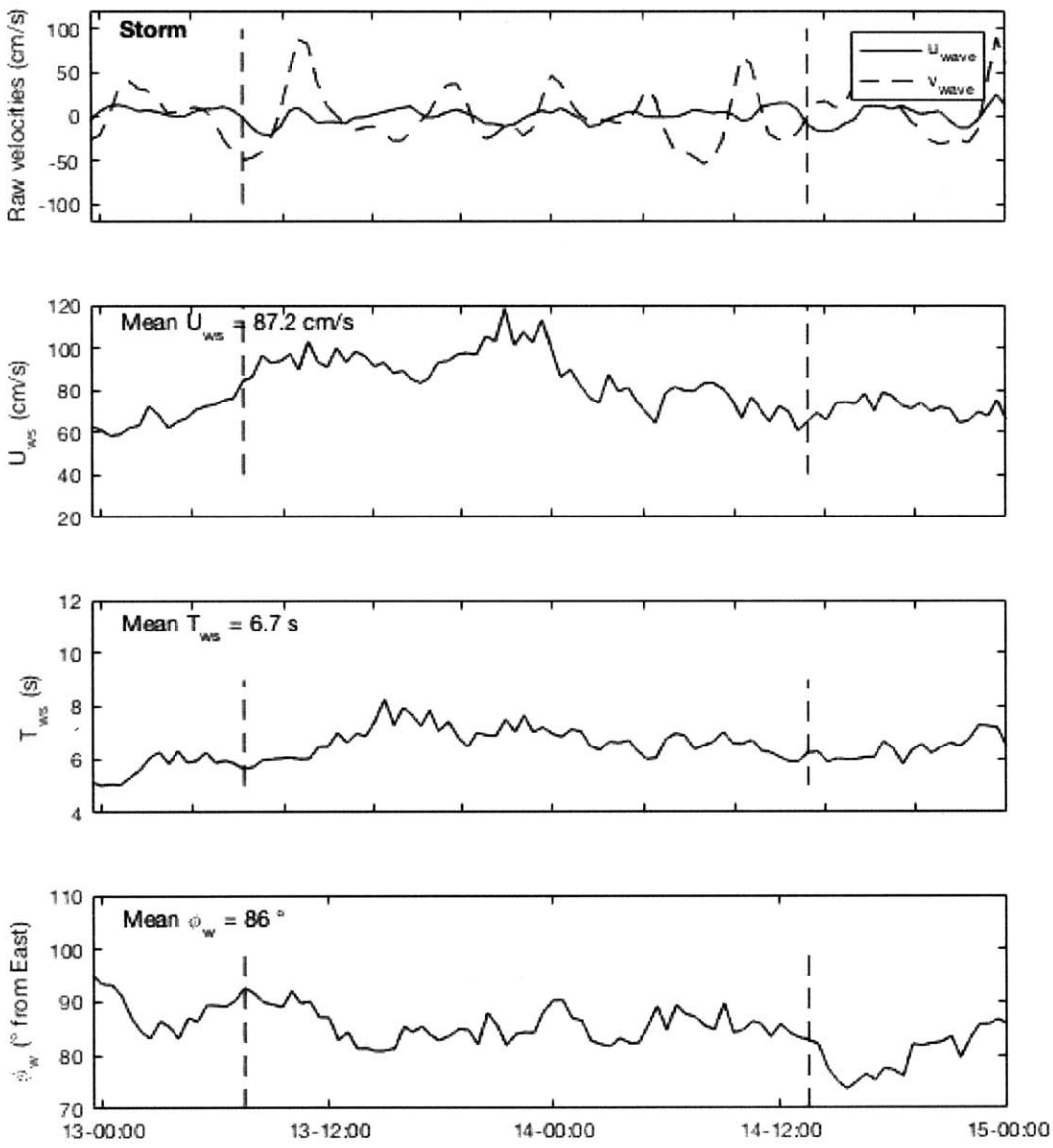

Figure 2.3.8: Characteristic wave properties for T61 during the storm interval. The vertical dashed lines indicate the range over which the storm was observed. u_{wave} and v_{wave} on the plot correspond to $\tilde{u}$ and $\tilde{v}$ respectively in the text.

2.4 Field Data Issues

Whilst processing the velocity data, it appeared that some of the time intervals studied (especially over the intervals with the larger water depth changes: during the spring tide) produced odd results which didn't have any physical explanations. Hence, the variation of the wave period during the spring tide as seen in Figures 2.2.4 (**b.**) and 2.3.7, or the "truncated" velocities during the storm in Figure 2.3.4 are instances in which the reliability of the data produced by the sensors was questioned. When comparing the depth variation with time over the month long recording period with the height of the pressure and velocity sensors, it became apparent that the velocity sensors were occasionally out of the water (see Figure 2.4.1). Whereas for T61 this problem occurred only during the spring tides, when the large tidal amplitude caused particularly low water levels to leave the sensor exposed, T62 and T65 suffered considerable loss of data. As the two sensors were also the ones closest to the inlet, it is highly possible that the additional flows coming in and out of Katama Bay on the same tidal cycle than the east-west currents along South Beach could have contributed to the amplification of depth variation. From Figure 2.4.1 it appears that the pressure sensor was almost always in clear water, and only the velocity sensors were affected by this issue. It would have hence been expected for the sensors to stop recording data, or to measure zero velocities when above the water surface. However, looking at 30 seconds intervals during the spring tides for T61 (see Figure 2.4.2), negative velocities were being recorded over intervals of several seconds. The erratic behaviour of the measurements taken at these times (highlighted by the red boxes in this Figure) contrasts with the smoother variations of the velocity when the sensor is in the water, and by overlapping both the depth plots and the velocity plots we can correlate the two sets of information quite well, proving that the anomalous velocities correspond to the lower water level values, or when the sensor is under the trough of a wave. The absence of sensor warnings however, or obvious gaps in the data, lowers the reliability of the submerged measurements made around the emerged ones. These exposures of the velocity sensors to the surface explain the anomalous raw velocities in Figure 2.3.4: the errors came up as the current direction was expected to be towards the west, so during the ebb tide when the water depth was decreasing. As the water levels dropped, the velocity sensors came out of the water and output random values. On the flood tide however, with increasing depth, the sensors were submerged again,

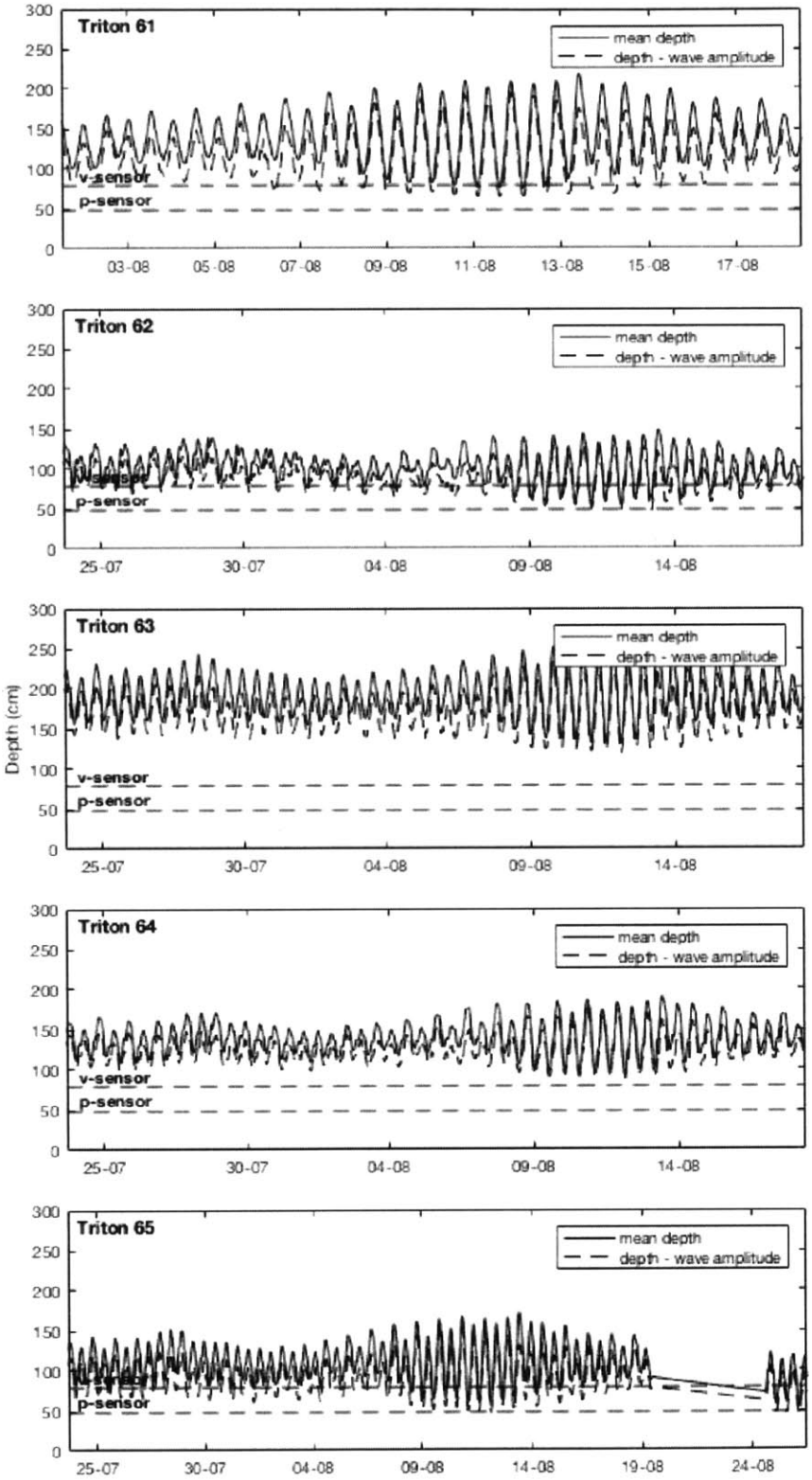

Figure 2.4.1: Depth variation with time for all sensors deployed around Katama Inlet in two meters average depth. The height of the sensors was compared in each case to the depth, as well as to the $h - a_s$ at each half hour.

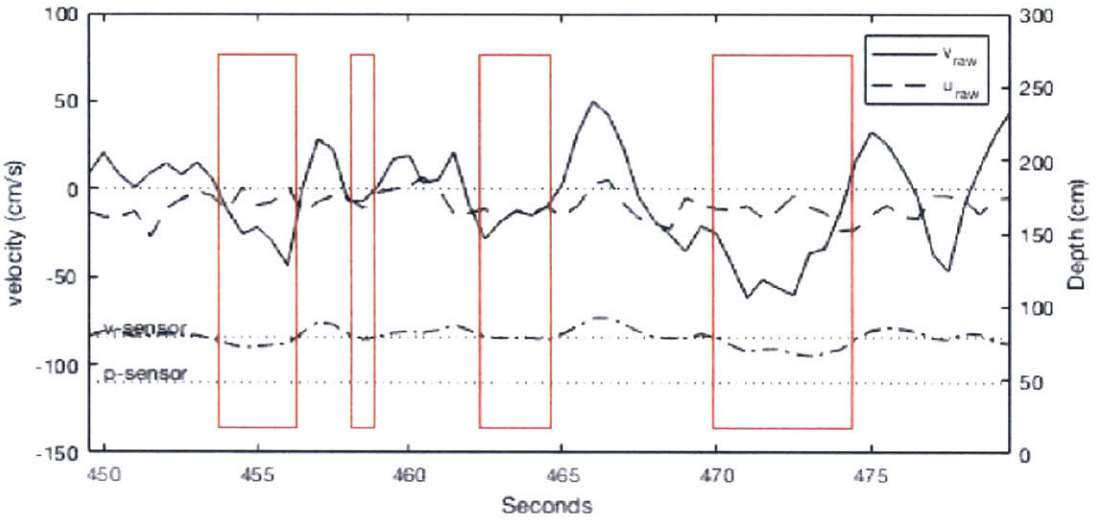

Figure 2.4.2: Velocity and depth plot over four wave periods during the neap tide for T61, showing the velocity sensor out of the water for intervals lasting several seconds.

and hence provided reliable data. The oscillations in the period data however, observed in both the velocity and the pressure analysis, cannot necessarily be explained just by the sensor height relative to depth issue, as the pressure sensors were always in the water for T61 (see Figure 2.4.1).

We have shown that the degree of agreement between the two measuring techniques is very good (see Section 2.3) in each of the studied intervals, and this is also true for the episodes during which the ADVs appear to be exposed. This correlation could be because the sensors are only affected over half the intervals (when the water is low), and the amount of data available overall compensates for these irregularities. Regardless, this agreement has enabled us, when there was doubt about the position of the ADV relative to the water level and some of the data output was dubious, to still use a mean value of the velocity data as it was close enough to those predicted by the pressure sensors to be realistic. The variations within the data however were ignored (so the period during the spring tide 48 hour interval was deemed constant and set to $T = T_s = 8.9s$). The agreement also allows for the results of velocity and period from the pressure calculations to be used with confidence, when the velocity data was severely contaminated (in sensors closer to the inlet like T62 or T65 for example).

2.5 Summary of Hydrodynamics

We have so far analysed the hydrodynamic properties of the field data collected along the south-east shore of Martha's Vineyard. These properties will be used to compute the net sediment transport. From the pressure data we have obtained the wave period $T_{\eta s}$, the significant wave amplitude a_s, and the orbital wave velocity amplitude both at the velocity sensor height z_u and at the bottom (U_{bm}). From the velocity data we have obtained the dominant wave direction ϕ_w, the wave velocity amplitude U_{ws}, the significant period T_s at z_u, the current direction ϕ_c and the current velocity U_c. Comparing the velocities at the velocity sensor height z_u from the pressure (U_p) and those measured by the ADV (see Table 2.2.2) we have shown that, as predicted, the pressure calculations overestimated the actual velocities by about $5-10\%$ (with the storm interval having the greatest variability, and the spring tide interval the least), due to assuming a unique direction of all waves during the 48 hour time interval. It is also shown in the same Table that the variation in orbital wave velocity with depth can be neglected as only marking a 3% change at most relative to the velocity computed at z_u, and hence the velocities used for the sediment transport calculations will be U_{ws} for each time interval.

Performing a similar comparison between the periods obtained with the pressure data and those obtained with the velocity data (see Figures 2.3.6 to 2.3.8 and Figure 2.2.4) in Table 2.5.1 we can confirm that the periods agree very well between both sets of data with a $0-3\%$ difference in the mean period over these intervals (with the spring tide interval having perfect agreement). We hence decided to also use the results from the velocity data for the sediment transport calculations, in order to be consistent with the velocity values used.

Table 2.5.1: Comparison of the wave period calculations from Sections 2.1 and 2.2.

(s)	Neap Tide	Spring Tide	Storm
$T_{\eta s}$	6.3	8.9	6.5
T_s	6.1	8.9	6.7

The similarity in the results obtained from both the velocity and the pressure data for the wave characteristics emphasizes the accuracy of either method when assessing these properties for sediment

transport, at least in this location. The velocity and pressure data analysis have also highlighted the correlation between the waves and the currents, with observations from Figure 2.2.7 showing that the wave surface height and the water depth have the same oscillation frequency, and from Figures 2.2.4 and 2.3.7 showing variations of the wave amplitude and velocity in phase with the water depth (and hence the tide and the currents as shown in Figure 2.3.3 for example).The magnitude of this variation δU_{wc} during the tidal period increases with the rougher conditions (see Table 2.3.2) and so, as this an important control on the wave shear velocity, and hence on the maximum shear velocity and on sediment transport, we will want to analyse how this increase affects sand motion over these intervals. As Figure **??** confirmed, the currents in the study area are strongly controlled by the tides. It therefore follows that the waves and the tides are strongly related, especially as the tides grow stronger (over the spring tides) and thus it is important to consider both together when looking at the sediment transport in the region. As a summary of the previous three sections, Table 2.5.2 presents the characteristic

Table 2.5.2: Summary of the characteristic wave and current specifications used in the sediment transport calculations.

	Neap Tide	Spring Tide	Storm
$\bar{U}_c$ (cm/s)	25.7	40.9	48.8
δU_c (cm/s)	21.5	30.5	23.5
U_{ws} ($z = z_u$) (cm/s)	52.3	39.1	87.3
δU_{ws} (cm/s)	8.1	13.9	11.7
T_s (s)	6.1	8.9	6.7
φ_{wc}	90.0	90.0	90.0

values for the currents and the waves which will be used in the sediment transport calculations, for each of the chosen time intervals. The angle between waves and currents was taken as 90°for simplification and as this was very similar to the results from Figures 2.3.2 - 2.3.4 and 2.3.6-2.3.8.

As the wave velocity variation with the tides has been shown to be important enough to be considered in the transport calculations, a synthetic data set based on the spring tide interval (which already featured the oscillation in the wave amplitude (Figure 2.2.4) and wave velocity (2.3.7)) was generated,

in order to better control the phase shift between the currents and the waves and study its effect more objectively. The scenarios show the waves and currents with a phase range of zero to three hours (0-90°) as well as when those are out of phase ($t_0 = 6hours$). The synthetic data was generated from the values displayed in Table 2.5.2, with

$$U_{c,synth} = \delta U_c cos(\frac{2\pi t}{T_t}) \tag{25}$$

and

$$U_{bm,synth} = U_{ws} + \delta U_{wc}(\frac{2\pi(t + t_0)}{T_t} \tag{26}$$

with t_0 a phase shift term set to zero for the waves and currents to be in phase, and to $6h$ for them to be out of phase. The resulting data sets are presented in Figure 2.5.1 and show an obviously idealised version of the real behaviour of the waves and the currents: the tidal asymmetry has disappeared and the current velocity magnitude is overall greater than in reality. This is because the maximum current velocity was chosen when identifying representative values of the dataset in Section 2.4 .

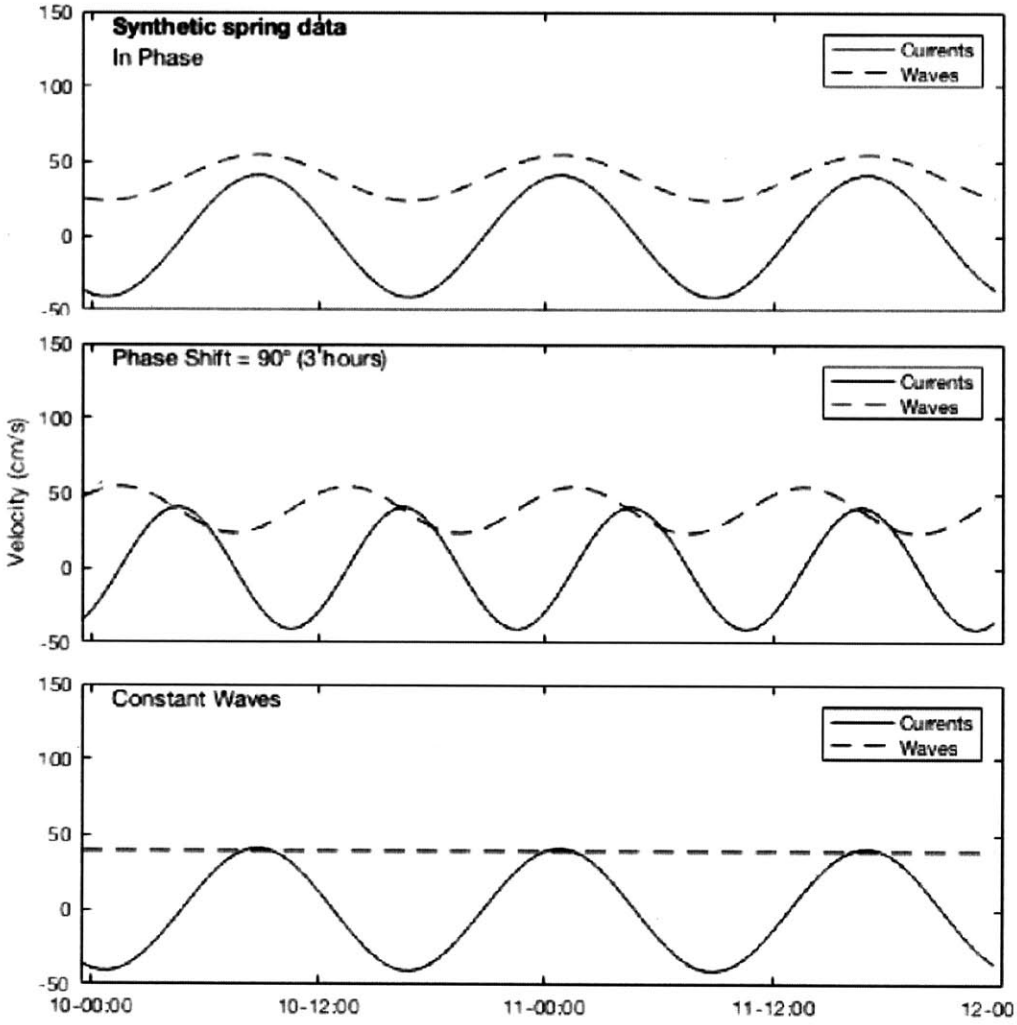

[h!]

Figure 2.5.1: Synthetic data computed from the mean wave characteristics and the maximum current velocity (from the hydrodynamic analysis), idealising three scenarios in which the waves and currents were in phase (**a.**), out of phase (**b.**) or unrelated (**c.**).

3 Sediment Transport Calculations

Sediment transport calculations have mostly been studied through two main methods. One follows an energetics approach developed by *Bagnold* (1963) and considers the flow to be expending energy to move the sediments (through turbulent diffusion for suspended load, and grain to grain interactions for bedload (*Bailard*, 1981)). The other uses a traction approach, considering bottom shear stress (estimated from a dimensionless friction factor which itself depends on the wave and current conditions) as the critical parameter instigating sediment uplift and hence transport (*Swart*, 1976; *Madsen and Grant*, 1976). We will here use the latter approach and study several scenarios to compare the effects of wave and current action on sediment transport in different tidal and meteorological environments.

First we used the data from the hydrodynamic analysis to evaluate what the transport was likely to be over the three intervals (neap, spring and storm variations) studied in Section 2. The computed time series of U_c, $U_{bm} = U_{ws}$ and T_s (displayed in Figures 2.3.6 to 2.3.8) were used as the input data into the transport calculations, for what we will call the "real data". The synthetic time-series derived in Section 2.5 were also studied, with $t_0 = 0 - 3hours$, and compared, for thoroughness, to a scenario in which the waves were constant in time (also shown in Figure 2.5.1).

3.1 Wave-Current Interactions

As the sediment transport calculations were based solely on the hydrodynamics computed above, the analysis focused on longshore net transport. An initial assumption of rough turbulent flow was also made, although verified further down in the calculations. The following methods for bedload transport were taken from *Madsen* (1993) and the same computations were used for each of the scenarios introduced previously. As both waves and currents were of interest in this study, wave-current interactions within the bottom boundary layer needed to be taken into account before computing the net transports. We first determined the wave-current friction factor,

$$f_{cw} = C_\mu \exp(5.5[\frac{C_\mu A_{bm}}{k_n}]^{-0.12} - 7.02) \tag{27}$$

with A_{bm} the wave's orbital amplitude at the seabed, k_n the Nikuradse equivalent bottom roughness (as we assumed rough turbulent flow, we took $k_n = d$ with $d \approx 0.05cm$ the sediment particle diameter), C_μ a factor used in combined wave and current environments,

$$C_\mu = \sqrt{1 + 2|\cos(\phi_{wc})|\mu + \mu^2} \tag{28}$$

and μ a parameter relating the current's importance relative to the waves',

$$\mu = \left(\frac{U_{*c}}{U_{*wm}}\right)^2 \tag{29}$$

The wave maximum shear velocity was then computed as

$$U_{*wm} = \sqrt{\frac{f_{cw}}{2}} U_{bm} \tag{30}$$

and from it we could easily obtain the maximum shear velocity,

$$U_{*m} = \sqrt{C_\mu} U_{*wm} \tag{31}$$

At this stage it was easy to verify the rough turbulent flow assumption by checking that

$$\frac{k_n U_{*m}}{\nu} > 3.3$$

We could now compute the bottom boundary layer thickness, in which the flow was affected by non linear friction processes due to the superposition of short lived wind waves with slower varying currents (*Madsen*, 1993):

$$\delta_{cw} = A \frac{\kappa U_{*m}}{\omega} \left(\frac{C_\mu}{\mu}\right)^P \frac{1}{16.3} \tag{32}$$

with

$$A = exp\Big(2.96\big(\frac{C_\mu A_{bm}}{k_n}\big)^{-0.071} - 1.45\Big) \tag{33}$$

and

$$P = \frac{\sqrt{C_\mu}}{2(\sqrt{C_\mu} - \sqrt{\mu})} \tag{34}$$

Having computed all the components controlling the current shear velocity we got:

$$U_{*c} = U_{*m} \frac{ln(\frac{z_r}{\delta_{cw}})}{ln(\frac{\delta_{cw}}{z_0})} \left[-\frac{1}{2} + \sqrt{\frac{1}{4} + \kappa \frac{U_c(z_r)}{U_{*m}} \frac{ln(\frac{\delta_{cw}}{z_0})}{ln(\frac{z_r}{\delta_{cw}})}} \right] \tag{35}$$

with $U_c(z_r)$, the current velocity, measured at the velocity sensor height above bottom, that is $z_r = z_u = 79cm$.

In order to try and solve the sediment transport equation for the conditions we have established in Section 2.5, we only had information regarding the current and wave velocities U_c and U_{wc} as well as their relative directions, but none concerning the current shear velocity, which is required to start solving for f_{cw}. In order to remedy this issue, an iterative approach was used to determine the current shear velocity at each half hour. This required making an initial assumption in which currents acted on their own, and the effect of waves was neglected. This first guess would enable us to proceed through equations 27 to 31 assuming $C_\mu = 1$, at which stage we could go back to updating f_{cw} (Equation 27) and the wave-current parameter and keep iterating using the first guess of shear velocity, until f_{cw} would converge to two significant figures. Once this was obtained, we could solve Equations 32 to 38 which would give us a second estimate of U_{*c} which then enabled us to reestimate the wave-current interaction parameters C_μ and μ and to start the second iteration from Equation 27 again. In this second iteration, Equations 27 to 31 would again be repeated until f_{cw} was considered stable before moving on to Equation 32. We continued iterating until U_*c converged to two significant figures (anything of higher accuracy would be over exploiting the data, considering the errors which were already accumulating from previous assumptions and the field data).

In the first iteration of this procedure we assumed the currents acted on their own to compute the wave-current friction factor as the convenient assumption of $\mu = 0$ could not be implemented as it led to a division by zero when calculating the boundary layer thickness. So we set

$$U_{*c,guess} = \sqrt{f_c} U_c \tag{36}$$

where f_c was the current friction factor,

$$f_c = \left(\frac{1}{4log(\, z_0/z_r \,)} \right)^2 \tag{37}$$

with $z_0 = k_n/30$ the location of the no slip boundary. These conditions were representative of a shear stress of

$$\tau_c = 2\frac{1}{2} f_c \rho U_c^2 \tag{38}$$

where the factor of "2" is introduced to account for the expected enhancement of the current shear stress by the presence of waves.

For each of the scenarios studied for the sediment transport described in Section 2.5 we compared the variation in the characteristic shear velocities U_{*c}, U_{*wm} and U_{*m} (see Figure 3.1.1). We observe that the maximum and wave shear velocities are very similar to each other whereas the current shear velocity is much smaller. This suggests that the waves are much more likely to instigate movement in the sand grains than the currents are, even in the idealised and current amplified conditions (Figure 3.1.2). The shear velocities resulting from the idealised data show a slight departure of U_{*m} from U_{*wm}, with U_{*m} getting slightly larger as the wave velocity is lower (and so lower U_{*wm}. This is because the relative effect of the waves on the currents is smaller when the former are smaller, which increases U_{*m} and thus the difference between U_{*wm} and U_{*_m}. Table 3.1.1 references the key values for the wave and current shear velocities in each scenario, based on the calculations from *Madsen* (1993). Whereas U_{*c} in the synthetic data averages out to zero (or close to) due to the symmetry of the data and hence cannot tell us much about the net transport without analysing the wave-current phase as well, the shear velocities for the real data seem to suggest clear motions of the sediment. The most obvious change in values is from the "calm" conditions, to the storm conditions. Both the wave and current shear velocities increase considerably from the former to the latter, due to the combined effect of the storm (higher winds and stronger waves) leading to an increase in wave velocities observed in Table 2.3.2 and of the spring tides (larger tides compared to the neap) which lead to higher current amplitudes and velocities. The greater importance of the waves relative to the currents to instigate

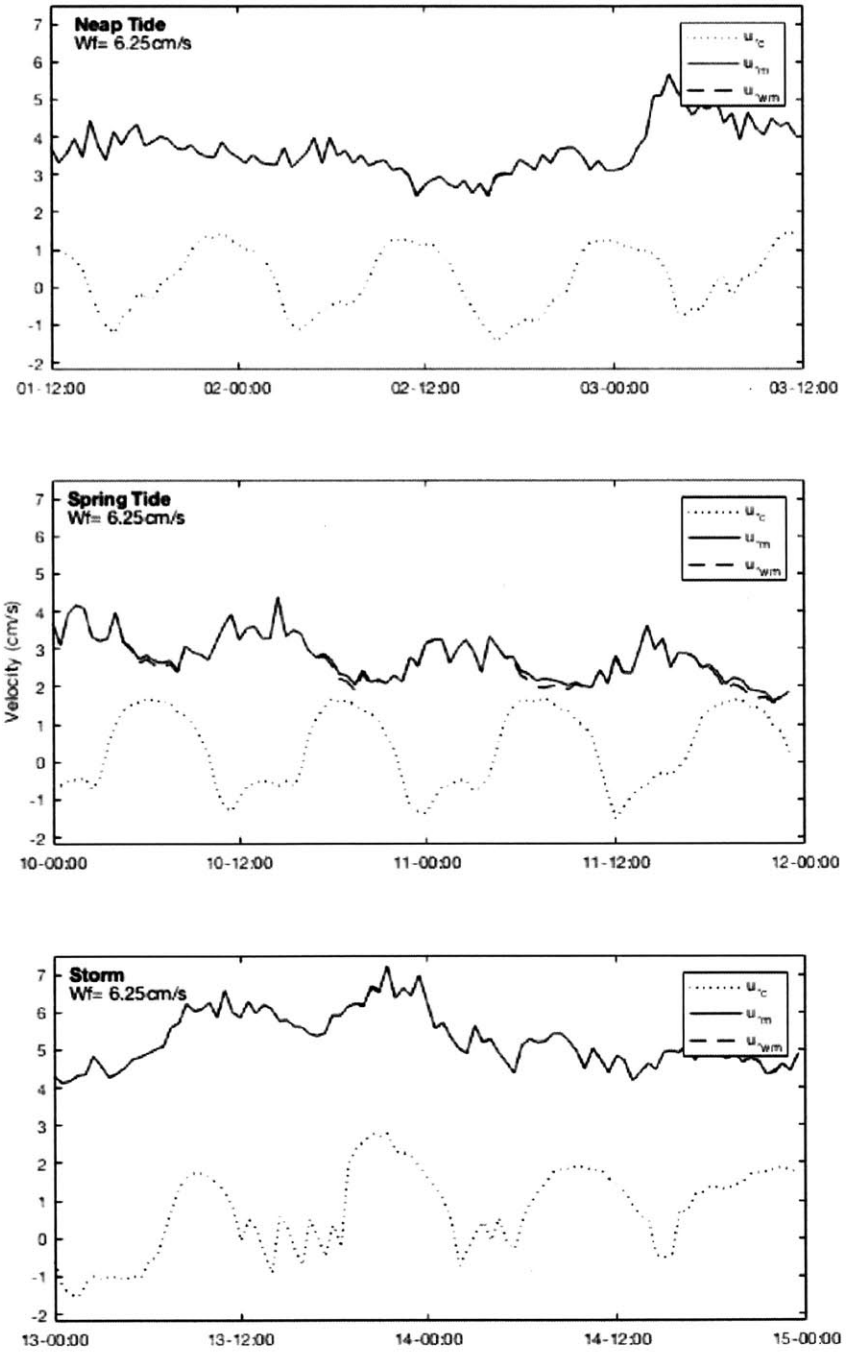

Figure 3.1.1: Shear velocities for the three real data scenarios (neap tides, spring tides and storm respectively).

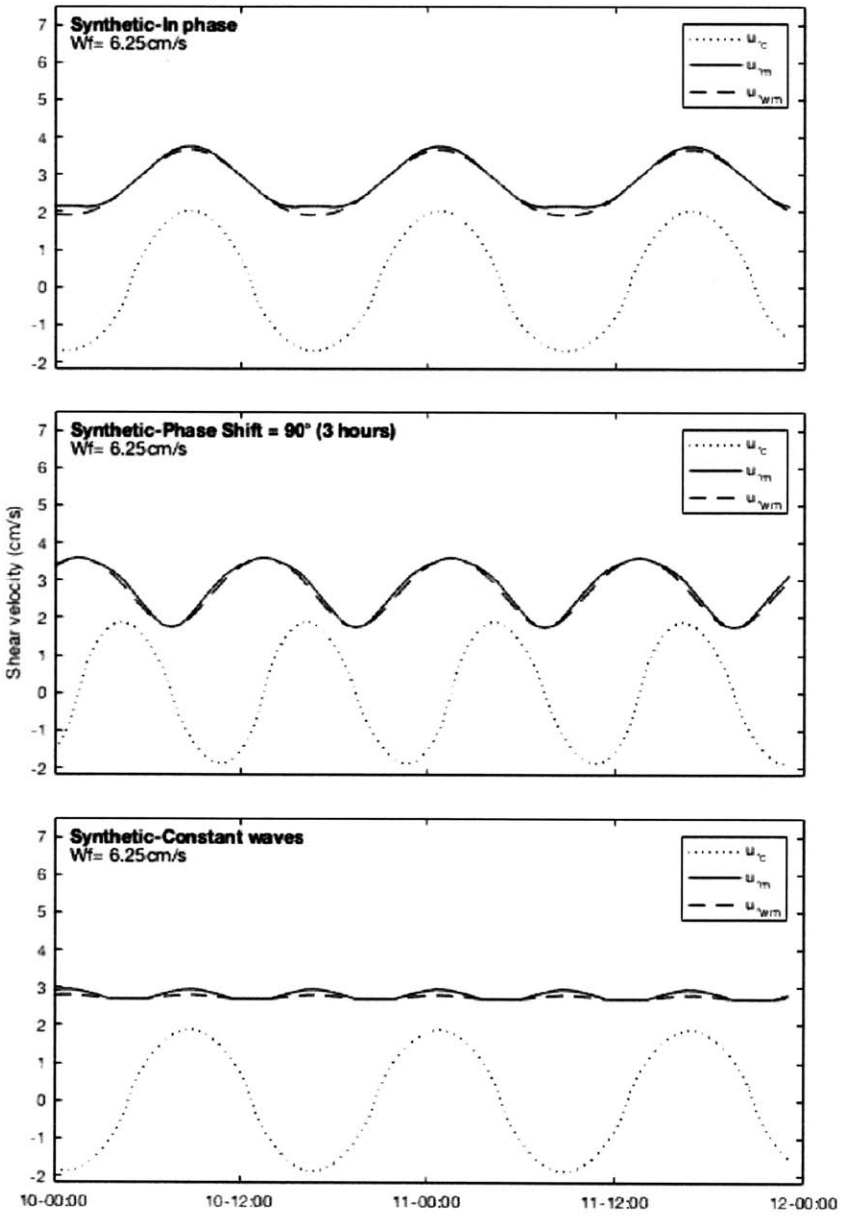

Figure 3.1.2: Shear velocities for the three synthetic scenarios based on data for the spring tides (in phase, out of phase and constant respectively). The current velocity used was the maximum current velocity computed from the velocity data for the spring tide, hence the transport rate is expected to be an overestimate of the reality.

Table 3.1.1: Shear velocity characteristics and variations for each of the studied scenarios in sediment transport, both based on real and synthetic data.

Shear Velocities (cm/s)	Real Data			Synthetic Data		
	Neap Tide	Spring Tide	Storm	In Phase	90° out of phase	Constant
$U_{*c,mean}$	0.230	0.350	0.730	0.015	0	0
$U_{*c,min}$	-1.450	-1.530	-1.550	-1.700	-1.900	-1.900
$U_{*c,max}$	1.480	1.710	2.790	2.030	1.900	1.900
$U_{*wm,mean}$	3.66	2.73	5.26	2.7	2.7	2.74
$U_{*wm,min}$	2.4	4.4	4.14	1.9	1.8	2.7
$U_{*wm,max}$	5.66	1.56	7.22	3.6	3.6	2.8

sediment transport was confirmed by the comparison of the critical shear velocity for motion $U_{*critical}$

$$U_{*critical} = \sqrt{(s-1)gd\psi_{critical})} \tag{39}$$

with

$$\psi_{critical} = 0.095S_*^{-2/3} + 0.056(1 - \exp(-S_*^{0.75}/20)) \tag{40}$$

and S_* the sediment fluid parameter, with $d = 0.05cm$,

$$S_* = d/4\nu \sqrt{(s-1)gd} \tag{41}$$

and the value of the current shear velocity $U_{*c,alone}$ during the spring tide, with $U_{*c,alone}$ computed as in the initial guess of the sediment transport rate iteration, without being increased by a factor of two. The results, plotted in Figure 3.1.3, show that $U_{*c,alone}$ never reaches $U_{*critical} = 1.62cm/s$, and show that sediment transport would not be possible in the present study, if the currents were acting alone and there was no influence from waves.

At the same time as the calculations were made, the settling velocity w_f of the sediment was computed, to assess any possible contribution of suspended sediment transport to the total transport. It was found, using

$$w_f = \frac{S_*}{5.4 + 0.92S_*} \sqrt{(s-1)gd} \tag{42}$$

that sediments settled too quickly relative to the shear velocities for there be any suspended sediment

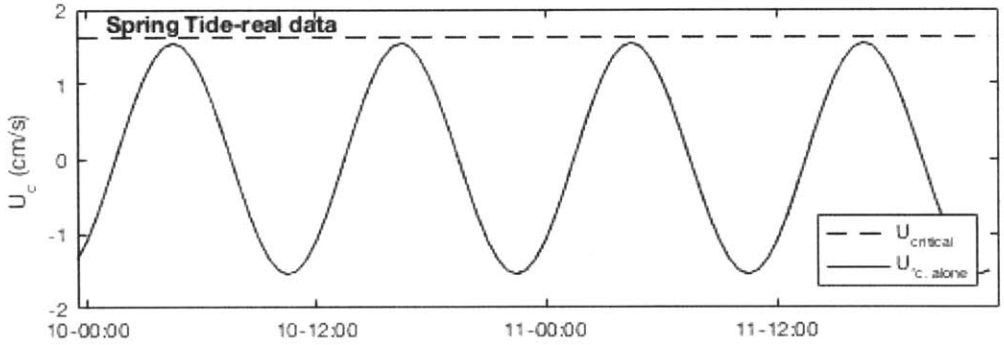

Figure 3.1.3: Critical and current shear velocities computed during the spring tide interval, with $U_{*c,alone} < U_{*critical}$ implying that another source of energy is needed in order to instigate sediment transport.

transport in the neap or spring tides intervals (w_f is presented on each plot in Figures 3.1.1 and 3.1.2, and for both these intervals (and hence in the synthesized data) was greater than U_{*m}). During the storm however, due to the sudden jump in the wave velocity U_{ws} and U_{*m} increase to $6.5 - 7\ cm/s$, the latter becomes greater than the settling velocity w_f for a few hours and suspension could therefore occur in theory at those times. Due to the minimal amount of time in which these conditions occur, and even then, the very small difference between w_f and U_{*m}, we assumed that all transport in the study area, during July-August 2014 was due to bedload movement and suspended load was negligible.

3.2 Net Tidal-Period Averaged Sediment Transport

Once U_{*c} and U_{*wm} were ascertained, we assessed the net bedload sediment transport vector and evaluated sediment transport both in the wave direction (x-direction) and 90°to the wave direction (y-direction) by first getting the Shields' parameter ψ_c, assuming a constant value for the angle of repose $\phi_m = 30°$,

$$\psi_c = \frac{U_{*c}^2}{(s-1)gd} \tag{43}$$

The wave-period-averaged bedload transport vector for combined wave-current flows at an angle ϕ_{wc} was given by *Madsen* (1993) as

$$\frac{\overrightarrow{Q_{wc}}}{\sqrt{(s-1)gdd}} = \frac{6}{\tan(\phi_m)} \psi_c^{3/2} \frac{U_{*m}}{U_{*c}} \left\{ \frac{3}{2} \cos(\phi_{wc}), \sin(\phi_{wc}) \right\} \tag{44}$$

for intense wave-dominated flows (corresponding to $\mu = {U_{*c}/U_{*m}}^2$ and ${U_{*critical}/U_{*m}}^2 << 1$. As seen from the results presented in Figures 3.1.1 and 3.1.2, these conditions for the applicability of Equation 44 are satisfied by our hydrodynamic scenarios over most of the tidal period.

This expression was then simplified by dropping the x-component (pointing in the same direction as the waves, which in this case corresponds to the North, and hence to the cross-shore transport) as $\phi_{wc} = 90°$ and thus $cos(\phi_{wc}) = 0$. The calculations were then carried out for the scenarios described in Section 2.5, that is for the real data during the neap and spring tides, and during the storm, as well as for the synthetic data with waves being in varying phase relative to the currents. The results are presented in Table 3.2.1, with Figure 3.2.1 showing an example of how this varies with time. From this figure, the effect of the storm is quite blatant, with a sudden jump in the net

Table 3.2.1: Table summarising the results of the sediment bedload transport calculations, for each of the intevals studied. The net transport is taken as $\sum_{48h} Q_{wc}/48h$, with positive values towards the east and negative values towards the west. All transports were rounded to three significant figures.

Transport (cm^3/(cm.s))	Real Data			Synthetic Data		
	Neap Tide	Spring Tide	Storm	In Phase	90° out of phase	Constant
Net	0.007	0.009	0.054	0.015	0	0
	0.00	*0.29*	*6.71*	*0*	*1*	*1*
Minimum	-0.041	-0.045	-0.070	-0.038	-0.071	-0.066
Maximum	0.064	0.052	0.375	0.101	0.071	0.066

transport rate from $0.12\ cm^3/(cm.s)$ to $0.35\ cm^3/(cm.s)$ in the space of $12hours$ around the 14th August, corresponding to the time when the maximum shear velocity, the wave velocity and the wind speed peaked. Because the net transport rate during the storm event is over six times greater than the net transport rate during normal conditions either in the spring tide or in the neap tide, it would take about a week for the amount of sediment moved during that storm (lasting only a few tidal cycles) to be moved under normal conditions, making its impact on sediment transport in August 2014 quite considerable. The difference in transport between the spring tide and the storm intervals relative to the neap tide also highlights the difference in impact waves and currents can have in this field: the bedload transport rate only increased by 20% between the neap tides and the spring tides (Table 3.2.1), when the main difference between the two datasets is in the current shear velocity, which doubled its range during the spring tide. This is because between these two intervals, the waves have also become

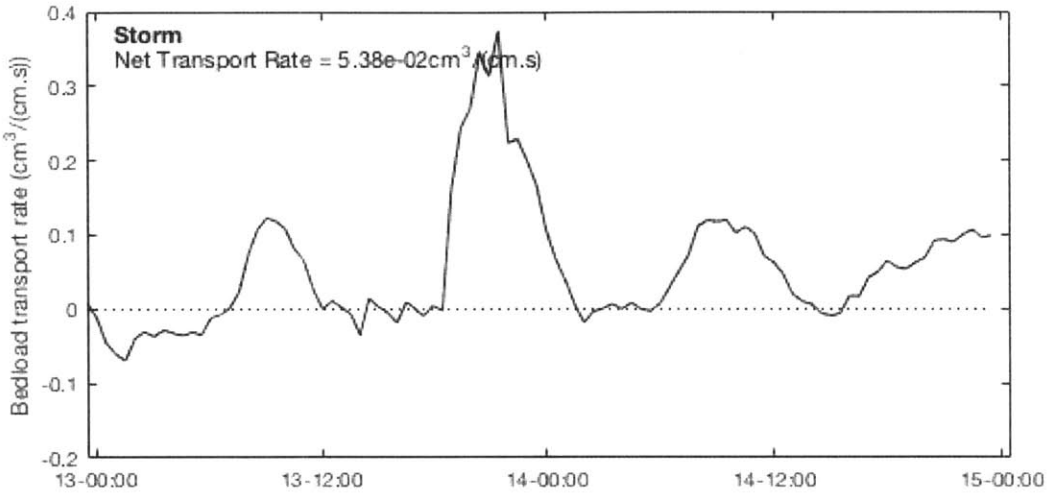

Figure 3.2.1: Bedload transport rate during the storm time interval, using the data obtained in Section 2.3. Note: the velocity sensor was in and out of the water at this time of the survey, hence some of the velocity measurements during the low tide were higher than expected, and may lead to a slight overestimate of the net transport rate in this case. Although the velocities corresponding to the peak should not have been affected by this, having been measured in high water levels.

smaller by 25% (see Table 2.2.1). This also shows that as the waves conditions remain more or less constant, the current strength has a smaller impact, being limited by the amount of sediment available for displacement. From the neap tide to the storm however, the transport rate increases by 630%. As the storm is also occurring during the spring tide the main difference between the two scenarios is the wave shear velocity which increases from $2.7cm/s$ during the spring tide interval to $5.6cm/s$ during the storm, highlighting the disproportionate effect of the waves on net transport compared to that of the currents. Indeed, because the waves are required to instigate transport, the stronger they are the more sediment can be moved by the currents.

The analysis of the phase shift between the waves and the currents shows that, at least for the conditions assessed here, the magnitude of the transport vector and its direction do depend on the phase. The results from Table 3.2.1 show that when there is a $90°$phase shift, the net transport rate is close to zero, and it then increases as the waves and currents come closer to being in phase (see Figure 3.2.2). This is because, when $phase = 90°$, as can be seen in Figure 3.1.2 the maximum and minimum U_{*wm} correspond to the times where $U_{*c} = 0$, hence the sediment can be picked up but

not moved along, occasioning a zero net transport rate. Because the data is idealised, the rest of the

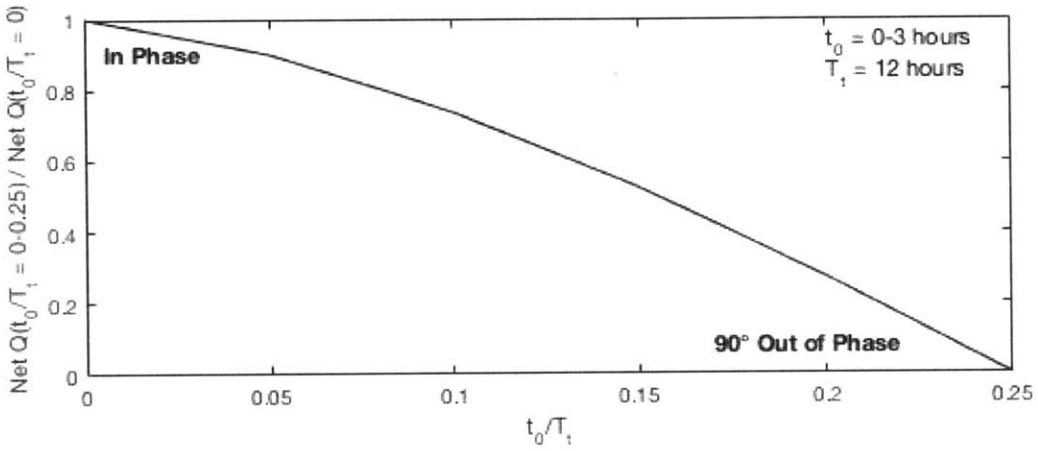

Figure 3.2.2: Normalised bedload transport rate as a function of the wave-current phase, with t_0 ranging between 0 to 3 hours (leading to a 90°phase shift).

time the transport rate is symmetric and overall comes to zero. As the phase shift decreases however (so waves and currents come closer to being in phase), $U_{*wm,max}$ moves away from $U_{*c} = 0$ and the net rate can increase to its maximum value obtained when the two are perfectly in phase (or out of phase). The direction of the net transport is also completely dependent on the shift: if the high wave velocities coincide with the high current velocities (or flood tide), the net transport occurs towards the east. If the waves are out of phase with the currents however (high wave velocities coinciding with the ebb tide), the net transport occurs towards the west. This again shows the disproportionate importance of the waves on sediment transport relative to the currents, as it is the timing of the wave velocities which control the transport direction and magnitude, and not the opposite (or the sediments would be moving eastward regardless of the phase as the currents are asymmetric). Finally, the net bedload calculations for the real data verify our original expectations that sediment is predominantly moving eastward along South Beach, towards Katama Inlet, matching the observations made from the satellite imagery in Figure 2.1.2 which showed its eastward migration. The fact that the transport towards the east dominates, regardless of the tidal (neap or spring) or meteorological (storm or not) conditions is another strong indicator of the current asymmetry.

4 Conclusions

The study of field data in shallow water by Katama Bay has covered several aspects of sediment transport calculations and the hydrodynamics associated with it. Despite some erroneous velocity measurements, reliable alternatives were used to fit the missing data and the following conclusions can be drawn:

1. Based on meteorological and water depth data, three key intervals with varying conditions of interest for sediment transport were identified: one characterising the neap tides (1st-3rd August), one characterising the spring tides (10th-12th August), and one characterising a storm (13th-15th August).

   The neap tides had a lower mean water level, smaller tidal amplitude and relatively constant significant wave height, period and velocity amplitude. The spring tides had a mean water level about 5% greater than the neap tides, a larger tidal amplitude and oscillating significant wave height, period and velocity amplitude, in phase with the currents. During the storm, which overlapped with the spring tides, the significant wave height and velocity doubled relative to the other two intervals.

2. The pressure data showed the water depth varying with 12.5 hour semi-diurnal period. Slow variation of the wave height showed a similar pattern particularly visible during the spring tide. Wave characteristics and orbital velocities were also computed. Two methods were used for the latter: using the surface spectra, or assuming representative characteristics and bulk translating the waves down to the sensor height. Both methods assumed unidirectionality of the waves and were hence expected to overestimate the total velocity slightly. In both cases the depth variation of the velocity was shown to be negligible (less than 5%) allowing for direct sensor measurements to be used and the results for the two methods were quasi identical (with a 2% overestimate from the bulk method).

3. The velocity data showed a tidal asymmetry in the tide-dominated currents, with the flood tide being between $30 - 190\%$ stronger than the ebb tide, and the greatest difference observed dur-

ing the spring tides. It also showed a net increase in wave orbital velocity between the neap tides and the storms, along with an increasing tidal variation (+70% between the neap and the spring tide). The wave period and velocities obtained from the velocity data showed excellent agreement with those obtained from the pressure data (within 10%), with the latter slightly overestimating the actual measurements due to assumed unidirectionality, as expected. This correlation between the two datasets confirmed that in shallow water, pressure data can represent velocity conditions within a high degree of accuracy, and both sets of measurement are interchangeable. The velocities also confirmed the tidal variation of the waves, by showing a semi-diurnal oscillation frequency in the wave height, emphasized during the spring tide.

4. The sediment transport over this interval was only due to bedload transport as $U_{*m} < w_f$ by at least 15% (neglecting the peak of the storm), and the waves were required to instigate transport in all three conditions, with $U_{*c,alone} < U_{*critical}$ for all studied intervals.

5. The sediment transport model was based on the three intervals studied in the hydrodynamics to compare the effect of these tidal and meteorological conditions on net alongshore sediment transport rate. In all three scenarios the net transport was oriented towards the East, which is in agreement with the eastward progression of the inlet. The storm, even though being a much more episodic event than the neap and spring tides, increased the average transport rate by about 600% due to the higher wave shear velocities, which were the greatest change between the conditions, showing that the waves have a larger effect on the amount of sediment which can be moved than the currents and are thus critical for sediment transport.

6. When analysing the effect of phase on the sediment transport it was observed that a phase shift ranging from 0° (in phase) to 90° (3 hours apart) affected net transport by 100%, with no net transport occurring for the 90° phase shift, and this net transport progressively increasing with the decreasing phase until reaching its maximum when currents and waves were either in or out of phase. The direction was still controlled by the dominant wave velocities, with the net transport going in the direction of the current at the time when the wave orbital velocities were the greatest.

References

Amoudry, L.O., and A.J. Souza (2011). Deterministic coastal morphological and sediment transport modelling: a review and discussion. *Rev. Geophys.*, *49*, RG2002.

Bagnold, R. A. (1963). Mechanics of marine sedimentation. In Hill, M.N. (Ed.), *The sea*,*3*(528), (pp. 4188–4194).

Bagnold, R.A. (1966). An approach to the sediment transport problem from general physics. *Geol. Surv. Prof. Paper*, *422*(1).

Bailard, J.A. (1981). An energetics total load sediment transport model for a plane sloping beach. *J. Geophys. Res.*, *86*(11), 10938–10954.

Camenen, B. and P. Larroudé (2003). Comparison of sediment transport formulae for the coastal environment. *Coast. Eng.*, *48*, 111–132.

Chan-Shu, Y. (1986). On Bagnold's sediment transport equation in tidal marine environments and the practical definition of bedload. *Sedimentology*, *33*(4), 465–487.

Dean, R.G., and R.A. Dalrymple (2004). *Coastal processes with engineering applications*, Cambridge University Press.

Delft Hydraulics (2007). User Manual Delft3D-FLOW: WL. *Delft Hydraulics*.

Duane, D.B., (1970). Tracing sand movement in the littoral zone: Progress in the radioisotope sand tracer (RIST) study. *U.S. Army Corps Eng. Coastal Eng. Res. Cent., Misc. Pap. 4?70.*

Einstein, H.A., (1972). Sediment transport by wave action. *Coast. Eng. Proc.*, *1*(13), 933–952.

Hoefel, F., and S. Elgar (2003). Wave-induced sediment transport and sandbar migration.*Science*,*299*(5614), 1885–1887.

Grant, W.D. and O.S. Madsen (1979). Combined wave and current interaction with a rough bottom.*J. Geophys. Res.*, *84*(C4), 1797–1807.

Grant, W.D., and O.S. Madsen (1986). The continental-shelf bottom boundary layer.*Annual Rev. Fluid Mech.*, *18*(1), 265–305.

Inman, D. L., Komar, P. D., and A.J. Bowen (1968). Longshore transport of sand. *Coast. Eng. Proc.*, *1*(11).

IPCC (2014). *Climate Change 2014: Synthesis Report. Contribution of Working Groups I, II and III to the Fifth Assessment Report of the Intergovernmental Panel on Climate Change* [Core Writing Team, R.K. Pachauri and L.A. Meyer (eds.)]. IPCC, Geneva, Switzerland, 151 pp.

Irish, J.L. and W.J. Lillycrop. (1997). Monitoring New Pass, Florida, with High Density Lidar Bathymetry. *J. Coastal Res.*, *13*(4), 1130–1140.

Komar, P. D. (1998). *Beach processes and sedimentation.* Upper Saddle River, NJ : Prentice Hall.

Le Roux, J.P. (2003). Wave friction factor as related to the Shields parameter for steady currents. *Sediment. Geol.*, *155*, 37–43.

Li, L. (2010). *A Fundamental Study of the Morphological Acceleration Factor* (Doctoral Dissertation, TU Delft, Delft University of Technology).

Longuet-Higgins, M. S., and R.W. Stewart (1964). Radiation stresses in water waves; a physical discussion, with applications. *Deep-Sea Res. Oceanogr. Abstr.*, *11*(4), 529–562.

Longuet-Higgins, M.S. (1970). Longshore currents generated by obliquely incident sea waves, 1. *J. Geophys. Res.*, *75*(33), 6778–6789.

Lou, J., and P.V. Ridd (1997). Modelling of suspended sediment transport in coastal areas under waves and currents, *Estuar. Coast Shelf S.*, *45*(1), 1–16.

Madsen, O.S, (1993). Wind stress, bed roughness and sediment suspension on the inner shelf during an extreme storm event. *Cont. Shelf Res.*, *13*(11), 1303–1324.

Madsen, O.S (x) Lecture on Basic Wave Theory. Personal Collection of O.S. Madsen, Massachusetts Institute of Technology, Cambridge, MA.

Madsen, O.S. (1993). Lecture on Sediment Transport on the Shelf. Personal Collection of O.S. Madsen, Massachusetts Institute of Technology, Cambridge, MA.

Madsen, O.S. and W.D. Grant (1976). Quantitative description of sediment transport by waves. *Coast. Eng. Proc.*, *1*(15), 1093–1112.

Svendsen, I.A (1984). Mass flux and undertow in a surf zone. *Coast. Eng.*, *8*, 347–365.

Swart, D.H. (1976). Predictive equations regarding coastal transports.

Tajima, Y. and O.S. Madsen (2005). Waves, currents and sediment transport in the surf zone along long straight beaches. *U.S. Army Corps Eng. Coastal Eng. Res. Cent.*.

van Rijn, L.C. (1984). Sediment Transport Part 1: Bedload transport. *J. Hydraul. Eng.*, *110*(10), 1431–1456.

Wang, P., Kraus, N. C., and R.A. Davis (1998). Total Longshore Sediment Transport Rate in the Surf Zone: Field Measurements and Empirical Predictions. *J. Coastal Res.*, *14*(1), 269–282.

Woods Hole Oceanographic Institution-Martha's Vineyard Coastal Observatory (2014). *Meteorological Data-Shore Lab and South Beach –Son3D-s (August)*[Data set]. Accessed on: http://www.whoi.edu/mvco/meteorological-data [13/02/2016].

Zhang, K., Douglas, B. and S. Leatherman (2002). Do storms cause long-term beach erosion along the U.S. East barrier coast?, *J. Geol.*, *110*(4), 493–502.